NASA TECHNICAL NOTE

NASA TN D-4504

NASA TN D-4504

DYNAMIC RESPONSE OF A FAMILY OF AXISYMMETRIC HAMMERHEAD MODELS TO UNSTEADY AERODYNAMIC LOADING

by Robert C. Robinson, Phillip R. Wilcox, Bruno J. Gambucci, and Robert E. George

Ames Research Center
Moffett Field, Calif.

NATIONAL AERONAUTICS AND SPACE ADMINISTRATION • WASHINGTON, D. C. • JUNE 1968

NASA TN D-4504

DYNAMIC RESPONSE OF A FAMILY OF AXISYMMETRIC HAMMERHEAD MODELS TO UNSTEADY AERODYNAMIC LOADING

By Robert C. Robinson, Phillip R. Wilcox,
Bruno J. Gambucci, and Robert E. George

Ames Research Center
Moffett Field, Calif.

NATIONAL AERONAUTICS AND SPACE ADMINISTRATION

For sale by the Clearinghouse for Federal Scientific and Technical Information
Springfield, Virginia 22151 – CFSTI price $3.00

DYNAMIC RESPONSE OF A FAMILY OF AXISYMMETRIC HAMMERHEAD MODELS TO UNSTEADY AERODYNAMIC LOADING

By Robert C. Robinson, Phillip R. Wilcox,
Bruno J. Gambucci, and Robert E. George

Ames Research Center

SUMMARY

The effects of boattail angle and diameter ratio on the unsteady aerodynamic loading on hammerhead launch vehicles were studied in wind-tunnel tests of 13 related dynamic models using the partial-mode model technique. The test Mach numbers ranged from 0.80 to 2.50 and the Reynolds numbers from 3.2×10^6 to 4.5×10^6 based on maximum diameter of the models. It was found that the unsteady aerodynamic loading was the result of two phenomena: buffeting due to separated flow and dynamic instability due to fluctuations between separated and attached flow.

INTRODUCTION

Many space payloads have a diameter greater than that of the final rocket stages used in launching, thus the launch configurations are "hammerhead" shapes. The geometrical transition between the payload and the rocket may cause a region of separated flow and, consequently, large fluctuations in the local pressure, such as those discussed in references 1 and 2. If those pressure fluctuations were correlated over a large area, a coupling between pressure and motion could develop that would transfer aerodynamic energy to the bending modes or rigid body dynamics of the complete vehicle. Fluctuations between separated and attached flow due to changes in angle of attack can, with the proper phasing, also transfer energy to the vehicle. Such phenomena have been observed in wind-tunnel tests of dynamic models, and the measured response and aerodynamic damping of several models have been reported in reference 3. Data from two of those configurations are included in this report. In reference 4 it is shown that the response of a free-oscillation model can be well predicted from pressure fluctuations measured on a static model if aerodynamic damping is included in the calculations.

The purpose of the present series of tests was to investigate the effect of a systematic variation of diameter ratio and boattail angle on the dynamic stability of partial mode models of hammerhead vehicles. Another objective was to correlate the stability of the models with the stability criterion of reference 5.

NOTATION

B	half-power bandwidth, Hz
$C_{m_{rms}}$	$\frac{\text{rms response moment at the node}}{qSD}$
D	maximum diameter
d	base diameter
f_n	model resonant frequency, Hz
M	free-stream Mach number
q	free-stream dynamic pressure
S	maximum cross sectional area
α	angle of attack
δ	boattail angle
ζ	ratio of damping to critical damping
ζ_T	tare damping ratio
θ	amplitude spectral density, degrees/$\sqrt{\text{Hz}}$
θ_5	amplitude spectral density at $f = 5$ Hz

MODELS AND TEST EQUIPMENT

Models

In the partial-mode model technique used in the present tests, rigid models are designed to simulate the portion of the full-scale vehicle where the important aerodynamic forces are expected to occur, as explained in some detail in references 4 and 6. The aerodynamic forces that contribute most to buffeting and instability of hammerhead shapes have been found to occur in the boattail area. Models for these tests were designed to simulate a mode in which the most forward node is behind the boattail. The portion of the model behind the node is attached rigidly to the support and the response of the active part of the model is measured at the node.

Two basic models with the same nose shape were used. One model had a maximum diameter of 11.19 inches (28.42 cm) and a base diameter of 7.00 inches (17.78 cm). The other model had a maximum diameter of 12.00 inches (30.48 cm)

and a base diameter of 6.00 inches (15.24 cm). The profile and dimensions of the larger model are shown in figure 1(a); the several combinations of boattail angle and diameter ratio that were tested are shown in figure 1(b).

Boattail angle and diameter ratio were changed by the use of "slip-ons" which were slid over the model base and brought to the correct position on the model where they were glued in place. Figure 2 shows the two types of slip-ons. With this technique changing, the model configuration was rapid and inexpensive.

The construction of both models was quite similar except that the rear cylindrical section of the large model, with a diameter ratio of 2, was metal because of the diameter limitations of the balance. Magnesium was selected for the cylinder to keep the model weight to a minimum. In general, the models were of lightweight sandwich-type construction. The inner shell was made of four layers of 0.004 inch (0.1016 mm) fiber glass cloth, and the outer shell of two layers of the same material; the filler was polyurethane foam having a specific weight of 2 lb/cu ft (31.4 N/m^3). Polyester resin was used sparingly as the binder. The smaller model, with a diameter ratio 1.6, was made entirely of the sandwich material except for a thin, short aluminum cylinder bonded to the aft end of the inner shell for mounting the model on the balance.

A 1-inch strip of number 40 carborundum grit, for inducing boundary-layer transition, appears as a dark band on the nose of the model in figure 3. The choice of grit size was based on the investigations reported in references 7 and 8.

Wind Tunnels

The tests were conducted in the Ames 14-Foot (4.27 meter) Transonic Wind Tunnel, 11-Foot (3.35 meter) Transonic Wind Tunnel, and 9- by 7-Foot (2.74 × 2.13 meter) Supersonic Wind Tunnel. The Mach number was varied from 0.80 to 1.40 in the transonic wind tunnels and from 1.55 to 2.50 in the supersonic wind tunnel. The corresponding Reynolds number range was 3.5×10^6 to 4.5×10^6 based on the maximum diameter of the models.

In all three facilities, the models were mounted on a sting attached to a movable strut. In the transonic wind tunnels, both the strut and the model plane of oscillation were vertical (figs. 3 and 4); whereas in the supersonic tunnel, although the plane of oscillation was vertical, the strut operated in a horizontal plane (fig. 5).

Balance

Details of the free-oscillation balance used in the tests are shown in figure 6(b). The model is secured to the model mount which is attached to a short cantilever resonant spring. The resonant spring serves a dual purpose: It fixes the model axis of rotation at the desired node line, and the output from its strain gages is the time history of the model motion about the center

of rotation. The air brake is used to limit the model deflection and thus keep the resonant spring bending stresses at a safe level. The maximum deflection of the model is controlled by a limit switch that energizes an air valve to operate the air brake. Figure 6(a) shows the relation of the fixed and active parts of a typical model to the sting and balance.

Instrumentation

The data from these tests can be classified into two groups: wind-off data used in evaluating the dynamic characteristics of the models and support systems, and wind-on data which were analyzed to evaluate the effects of configuration changes on the aerodynamic forces. Figure 7 shows the instrumentation used to record the model response during both wind-off and wind-on tests. In the "operate" position the standard termination is AC coupled to eliminate any bias due to static aerodynamic loads, thus making the entire dynamic range of the recording system usable for the dynamic response of the models. In the "calibrate" position DC is passed, permitting static calibration of the strain gage. The precise AC calibration signal, which was recorded simultaneously on all channels, was used as a voltage and frequency reference in the analysis of the recorded data.

Additional instrumentation required in the wind-off tests included a frequency response analyzer and a system for exciting the model. Figure 8 shows the arrangement for measuring the frequency response of a model. The output of the force gage in the impedance head and the output of the strain gage in the balance were sent to the frequency response analyzer which produced a log plot of amplitude ratio versus frequency. The same system was used in measuring the sting characteristics except that both inputs to the analyzer were taken from the impedance head. The dynamic characteristics of each model were checked before and after each wind-on test by recording a free oscillation decay. In the earlier tests the models were excited by hand tapping, but an improved technique was developed (fig. 9) in which a step input was produced when a weight hung from an elastic strap was released by cutting the connecting wire. This provided both a well defined input to the model and a check on the static calibration of the strain gage.

ESTIMATION OF TARE DAMPING

To evaluate the effects of configuration changes and test conditions on the aerodynamic damping, it is essential to have a good approximation to single-degree-of-freedom motion and a nearly constant, low level of tare damping. If the model frequency is too near a support frequency, the model response will contain two frequencies, and the effective damping of the model will be changed. To avoid this condition either the model frequency or the support frequencies may be altered. The model frequencies were changed by adding mass or by changing to a different resonant spring. The support characteristics were changed by tethering the sting (as shown in fig. 4), by suspending a weight from the sting, or by changing to a sting of different length.

A short sting with a high first-bending frequency was used for most of the tests in the 11-foot transonic wind tunnel. The frequency response for this sting (fig. 10) shows a first-bending frequency of 38 Hz, well above the desired model frequency of 20 Hz (full-scale frequency of 2.0 Hz). A frequency response plot for one of the larger models mounted on this sting is shown in figure 11 where it can be seen that at the model frequency of 19.2 Hz a single degree of freedom was very well approximated. At the sting frequency the deviation from the single-degree-of-freedom curve is only about 0.5 percent of the model's peak response. The corresponding free-oscillation decay for this model (fig. 12(a)) is smooth with $f_n = 20$ Hz and $\zeta = 0.016$. However, when the smaller models were mounted on the short sting, the small increase in model resonant frequency resulted in an uneven decay, as shown in figure 12(b). Analysis of this decay by the technique reported in reference 9 showed the model frequency to be 21 Hz with $\zeta = 0.035$. The interfering frequency was found to be 23.5 Hz. This unknown support mode is barely discernible in the sting frequency response (fig. 10). Fortunately the static instability of these configurations about the moment center lowered the wind-on resonant frequency below 20 Hz. Consequently interaction with the support was small as shown by the typical amplitude spectra of the wind-on response presented in figure 13. Because of the decreased frequency with wind on, it is estimated that the wind-on tare damping of the models which had wind-off frequencies above 20 Hz was about the same as for models with wind-off frequencies below 20 Hz, namely $0.012 \leq \zeta \leq 0.015$. Exceptions to this are models 3 and 11 which were tested on a different sting and had a very low level of tare damping. Table I lists the wind-off frequency and damping and the average wind-on frequency for all the models.

AERODYNAMIC EFFECTS ON MODEL RESPONSE

In the wind-on tests, the data acquisition procedure consisted in recording a 60-second time history of the model at fixed Mach numbers and angles of attack. Changes in Mach number and attitude were made with the models free to oscillate about the node line so that any large response confined to a narrow range of M or α could be detected. The model response was monitored continuously on an oscilloscope, and if any significant increases in amplitude were noted, data were recorded at those points in addition to those scheduled. If the model response exceeded a preset level, the brake was automatically actuated. In some cases response of the model was great enough to cause brake actuation before a record long enough for analysis could be obtained.

The random character of the model response is illustrated by the two typical time histories in figure 14. The amplitude distribution of the absolute values of the responses was determined by the technique described in reference 10. The data in figure 15 follow the normal distribution and therefore the amplitude distribution can be completely characterized by the root mean square. The rms of the strain-gage output was obtained by integrating over the full length of each record and was then reduced to a response-moment coefficient, $C_{m_{rms}}$. Figures 16 through 19 show the variation of $C_{m_{rms}}$ with Mach number at $\alpha = 0^\circ$ and 2° for all the models.

Six points for which the response was exceptionally large have been labeled "unstable" on figures 18 and 19. However, dynamic stability cannot be judged on the basis of amplitude alone as a large response can result from either negative aerodynamic damping or increased buffeting. A measure of the aerodynamic damping can be obtained from amplitude spectra such as those shown in figure 13. It can be shown (ref. 11) that for small damping the half-power bandwidth of the spectrum peak is related to the damping ratio by the following equation:

$$B = 2\zeta f_n$$

A bandwidth measurement which shows the net damping (tare damping plus aerodynamic damping) to be less than the tare damping is an indication of negative aerodynamic damping.

The variation of bandwidth with Mach number for the $D/d = 1.6$, $\delta = 17^\circ$ model at $\alpha = 0^\circ$ and 2° is shown in figure 20. The tare damping converted to bandwidth is also shown for comparison. At zero angle of attack, the net damping is much less than the estimated tare damping at $M = 1.00$, confirming that the large response for this test condition is due to dynamic instability. The bandwidth at $\alpha = 2^\circ$ shows a sharp drop at $M = 0.98$ and 0.99, indicating that a very narrow range of instability may exist at $\alpha = 2^\circ$ and $M \approx 0.985$.

The $D/d = 2.0$, $\delta = 20^\circ$ model was definitely unstable at $\alpha = 2^\circ$ as well as at $\alpha = 0^\circ$ (fig. 21). At $\alpha = 2^\circ$ and $M = 1.18$ the total damping approaches zero, whereas at the other Mach numbers it is several times greater than the tare damping for this angle of attack. For $\alpha = 0^\circ$, the response was so violent at $M = 1.25$ that a record long enough for analysis could not be obtained; however, the trend of the bandwidth data is toward zero damping for this test condition. The variation of bandwidth with angle of attack in figure 22 shows that instability occurred also at $M = 1.20$ and $\alpha = 1.4^\circ$.

Although the $D/d = 1.6$, $\delta = 20^\circ$ model was unstable at $M = 1.20$, $\alpha = 0^\circ$ in the 14-foot wind-tunnel tests, as reported in reference 1, it was stable in the 11-foot wind-tunnel tests. Figure 18(d) shows that the response at $M = 1.20$ was very low and bandwidth measurements indicated that the aerodynamic damping was positive for this model at all the test conditions.

To show more clearly the interrelated effects of diameter ratio, boattail angle, and Mach number, isometric plots were made showing $C_{m_{rms}}$ as a function of those parameters. Figure 23 shows such plots for diameter ratios of 1.25, 1.60, and 2.00 at $\alpha = 0^\circ$. For $D/d = 1.25$ the maximum response occurs between $M = 0.90$ and $M = 1.00$ forming a broad level ridge. The effect of boattail angle is negligible. At $D/d = 1.60$ (fig. 23(b)) there are two ridges. One is relatively low and broad with its maximum at $M = 0.95$ for all values of δ. It is considered to be the result of a high level of buffeting due to separated flow over the boattail. The other ridge, narrow and of large amplitude, is formed by the three unstable points. The two ridges coincide at $\delta = 10^\circ$ and $M = 0.95$. As δ is increased to 17°, the Mach number for instability increases to 1.0. There is a buffeting ridge between $M = 0.90$ and $M = 1.00$ for $D/d = 2.00$ also (fig. 23(c)), and one point of instability is at $M = 1.25$. The larger Mach number separation between the buffeting maximum and

the unstable point for this diameter ratio makes it more apparent that two different phenomena are involved. One is the buffeting due to separated flow and the other is the instability due to fluctuations between separated and attached flow. A similar plot for the $D/d = 2.0$ models at $\alpha = 2^{\circ}$ would show a smaller Mach number separation between the unstable point and the buffeting ridge.

A comparison of the three parts of figure 23 shows the differing effects of changes in boattail angle and diameter ratio. It is evident that although the boattail angle is a determining factor in the dynamic stability of a configuration, it has only a small effect on the buffeting level. Diameter ratio, however, has an important influence on both dynamic stability and buffeting level. There appears to be a minimum D/d below which instability does not occur for a given boattail angle, and there is a significant increase in buffeting with increasing diameter ratio.

The stability criterion of reference 5 is based on the pressure gradient in the boattail region computed from a theoretical pressure distribution and classifies configurations having maximum adverse pressure gradients between 0.2 and 1.8 as being "separated-unstable." The maximum adverse pressure gradients for the present 13 configurations varied from 0.33 to 2.23. The pressure gradients for the four dynamically unstable configurations fall in the separated-unstable range; however, eight other configurations in that range were stable, on the basis of data from these tests.

CONCLUSIONS

Results from wind-tunnel tests of partial-mode models of 13 related hammerhead configurations lead to the following conclusions:

1. Unsteady aerodynamic loading on launch vehicles with hammerhead payloads can result from two phenomena: buffeting caused by separated flow and dynamic instability due to fluctuations between separated and attached flow.

2. The Mach number and angle of attack at which dynamic instability occurs are influenced by both boattail angle and diameter ratio.

3. The buffeting level increases with diameter ratio but is insensitive to changes in boattail angle.

4. The stability criterion of NASA SP 8001 is conservative for configurations similar to those studied in these tests.

Ames Research Center
National Aeronautics and Space Administration
Moffett Field, Calif., 94035, Dec. 28, 1967
124-08-04-09-00-21

REFERENCES

1. Coe, Charles F.: The Effects of Some Variations in Launch-Vehicle Nose Shape on Steady and Fluctuating Pressures at Transonic Speeds. NASA TM X-646, 1962.

2. Coe, Charles F.; and Nute, James B.: Steady and Fluctuating Pressures at Transonic Speeds on Hammerhead Launch Vehicles. NASA TM X-778, 1962.

3. Robinson, Robert C.: A Wind-Tunnel Investigation of the Dynamic Stability of Axisymmetric Models With Hammerhead Noses in Transonic Flow. NASA TM X-787, 1963.

4. Cole, Henry A., Jr.: Dynamic Response of Hammerhead Launch Vehicles to Transonic Buffeting. NASA TN D-1982, 1963.

5. Anon.: NASA Space Vehicle Design Criteria, Buffeting During Launch and Exit. Vol. III: Structures, Part B: Loads and Structural Dynamics, Chapter 3: Launch and Exit, Section 1: Buffeting. NASA SP-8001, 1964.

6. Cole, Henry A.; Jr., Robinson, Robert C.; and Gambucci, Bruno J.: Detection of Flow-Field Instability in the Presence of Buffeting by the Partial-Mode Model Technique. NASA TN D-2689, 1965.

7. Holdaway, George H.; Mellenthin, Jack A.; and Hatfield, Elaine W.: Investigation at Mach Numbers of 0.20 to 3.50 of a Blended Diamond Wing and Body Combination of Sonic Design but With Low Wave-Drag Increase With Increasing Mach Number. NASA TM X-105, 1959.

8. Holdaway, George H.; and Mellenthin, Jack A.: Investigation at Mach Numbers of 0.20 to 3.50 of Blended Wing-Body Combinations of Sonic Design With Diamond, Delta, and Arrow Plan Forms. NASA TM X-372, 1960.

9. Wilcox, Phillip R.; and Crawford, William L.: A Least Squares Method for Reducing Free-Oscillation Transient Data. NASA TN D-4503, 1968.

10. Cameron, William D.: Hybrid Computer Techniques for Determining Probability Distribution. Presented at the International Symposium on Analogue and Digital Techniques Applied to Aeronautics (Liege, Belgium), Sept. 9-12, 1963, pp. 400-405.

11. Fêng, Yüan-chên: An Introduction to the Theory of Aeroelasticity. John Wiley and Sons, Inc., 1955, pp. 477-479.

TABLE I.- FREQUENCY AND DAMPING CHARACTERISTICS OF THE MODELS

Model	D/d	δ	Wind tunnel	Wind-off		Wind-on Average f_n, Hz
				f_n, Hz	ζ	
1	2.0	30°	11-foot	20.0	0.016	16.5
			9- by 7-foot	17.9	0.009	16.0
2	2.0	25°	11-foot	19.5	0.012	16.1
			9- by 7-foot	17.8	0.007	15.7
3	2.0	20°	11-foot	19.4	0.002	16.4
4	1.6	30°	11-foot	19.2	0.015	16.5
			9- by 7-foot	17.8	0.009	15.6
5	1.6	25°	11-foot	21.0	0.035	19.2
6 (ref. 3)	1.6	20°	11-foot	21.0	0.018	18.7
			14-foot	23.3	0.017	---
7	1.6	17°	11-foot	21.0	0.034	18.5
8	1.6	15°	14-foot	19.7	0.019	---
9 (ref. 3)	1.6	10°	14-foot	24.6	0.018	---
10	1.25	30°	11-foot	18.7	0.014	16.5
			9- by 7-foot	17.6	0.014	15.5
11	1.25	20°	11-foot	18.7	0.004	16.7
12	1.25	17°	11-foot	20.5	0.018	18.5
13	1.10	30°	11-foot	18.7	0.014	16.2
			9- by 7-foot	17.3	0.007	15.0

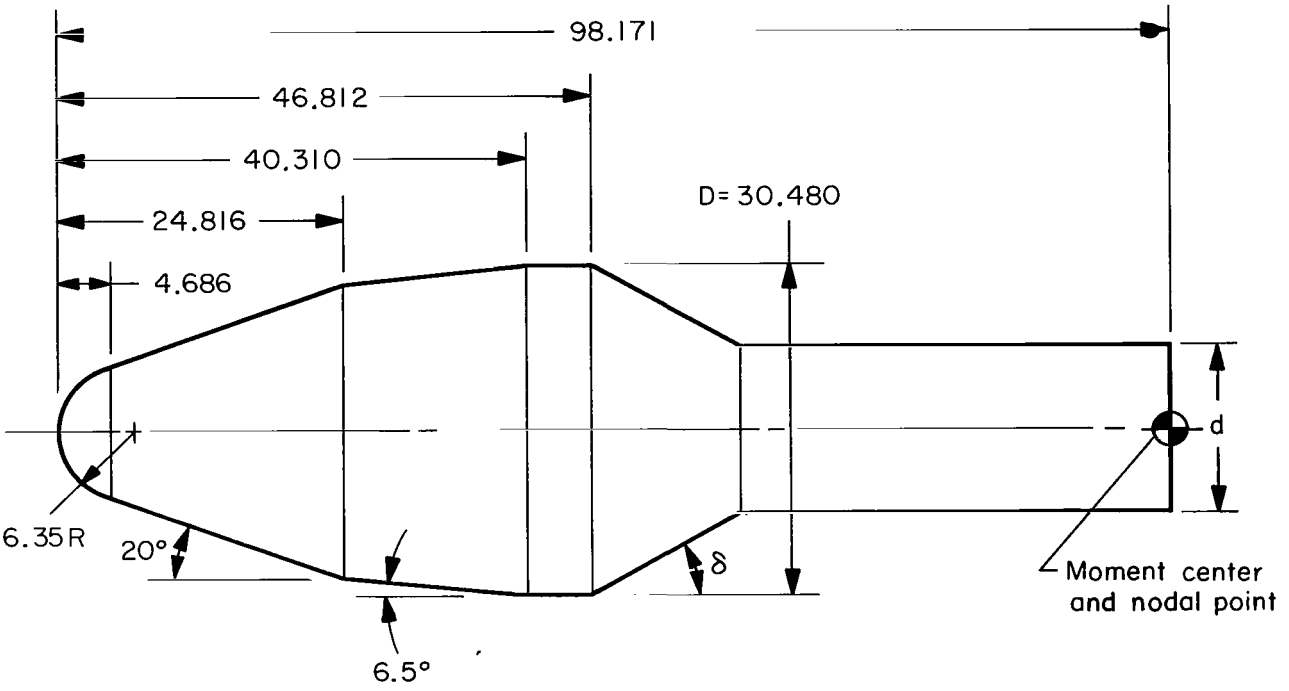

NOTE: All dimensions in centimeters

(a) Profile of the larger basic model.

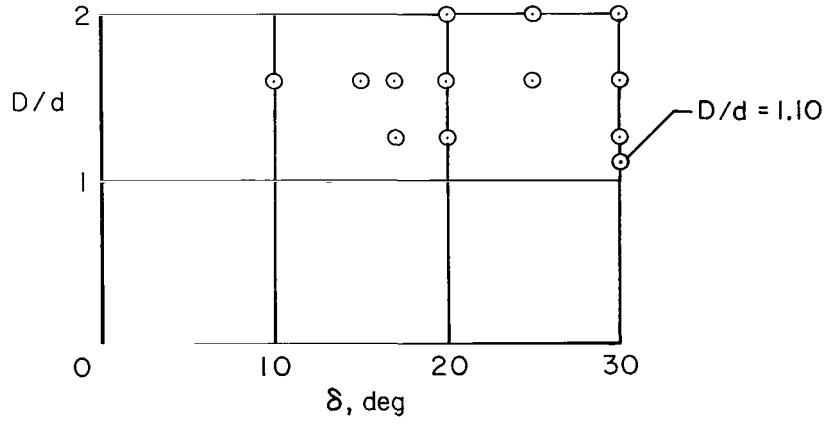

(b) Model configurations.

Figure 1.- Dimensions of a typical model and combinations of boattail angle and diameter ratio tested.

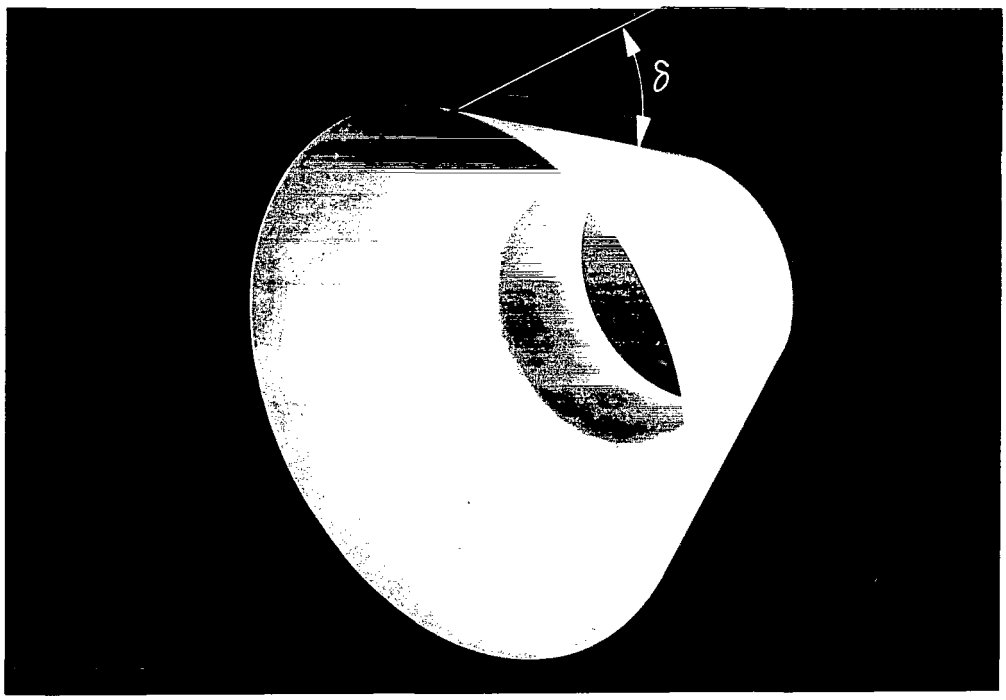

A-35637.1

(a) Slip-on for changing model boattail angle.

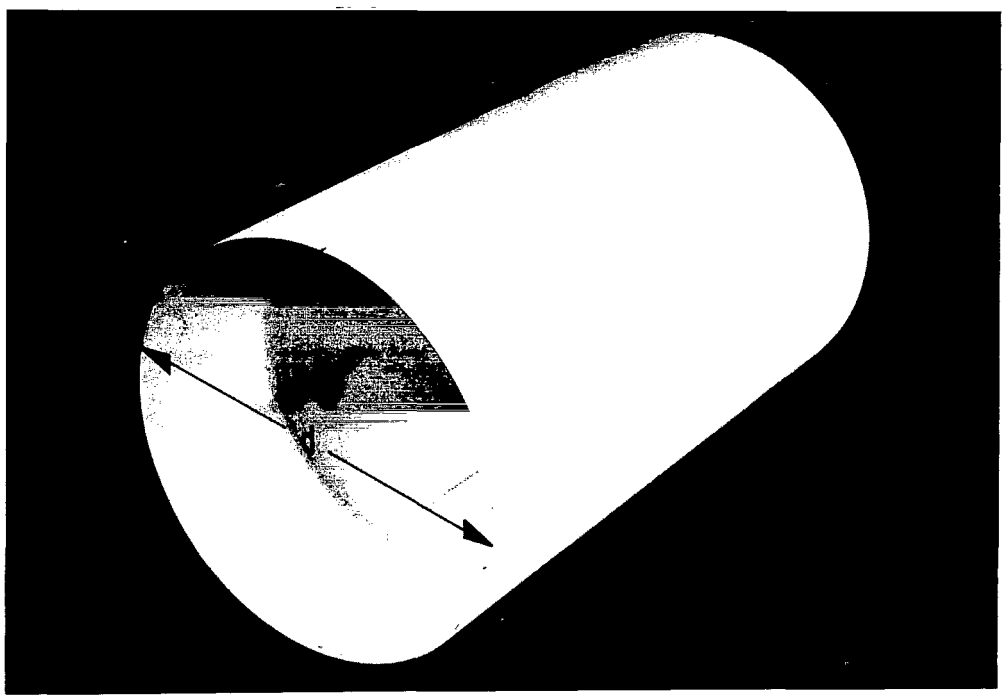

(b) Slip-on for changing diameter ratio. A-35638.1

Figure 2.- Typical slip-ons used to change model configuration.

Figure 3.- A model mounted in the 14-foot transonic wind tunnel. A-28132

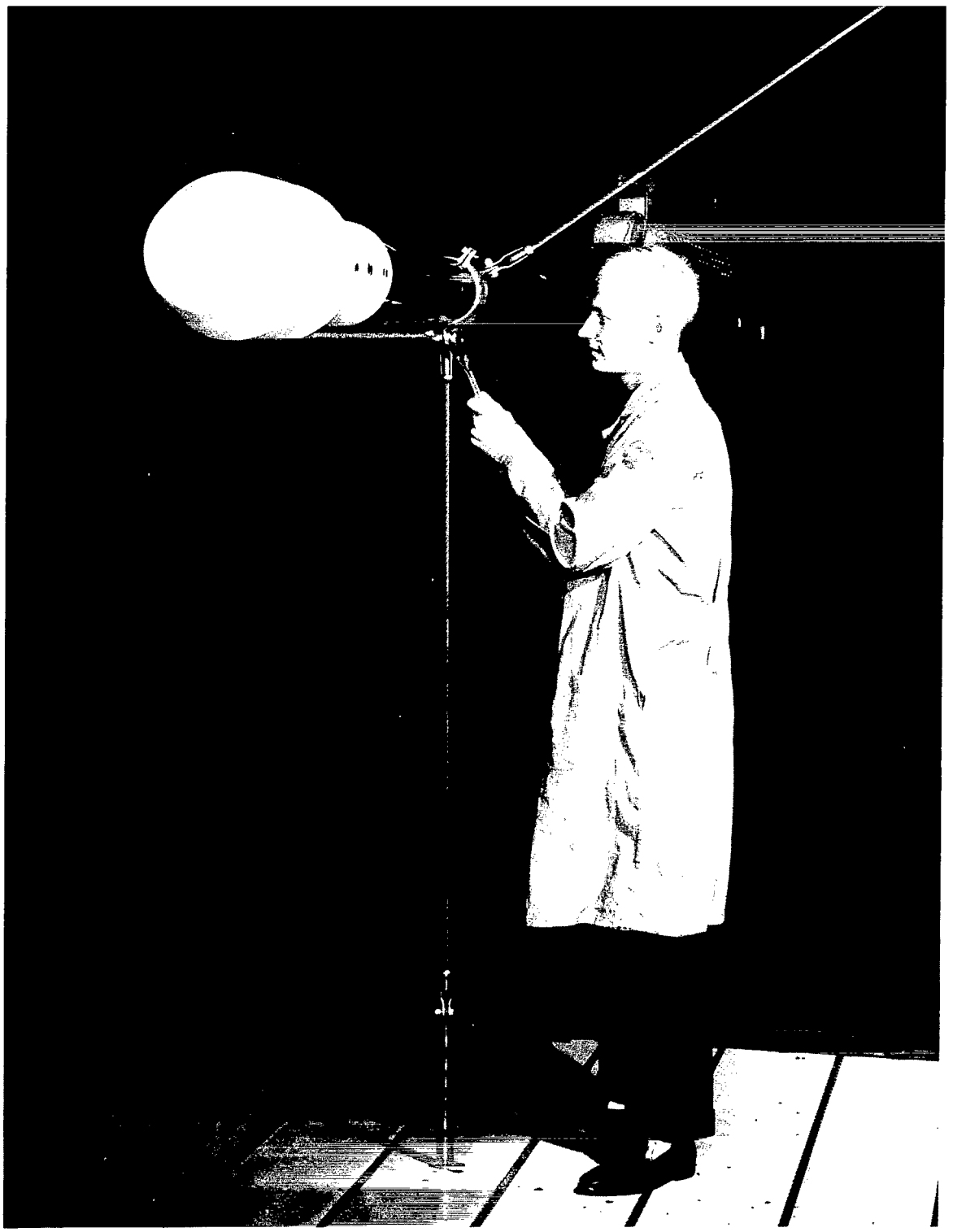

A-31348

Figure 4.- A model mounted in the Ames 11-Foot Transonic Wind Tunnel.

A-33875

Figure 5.- A model mounted in Unitary 9- by 7-foot wind tunnel.

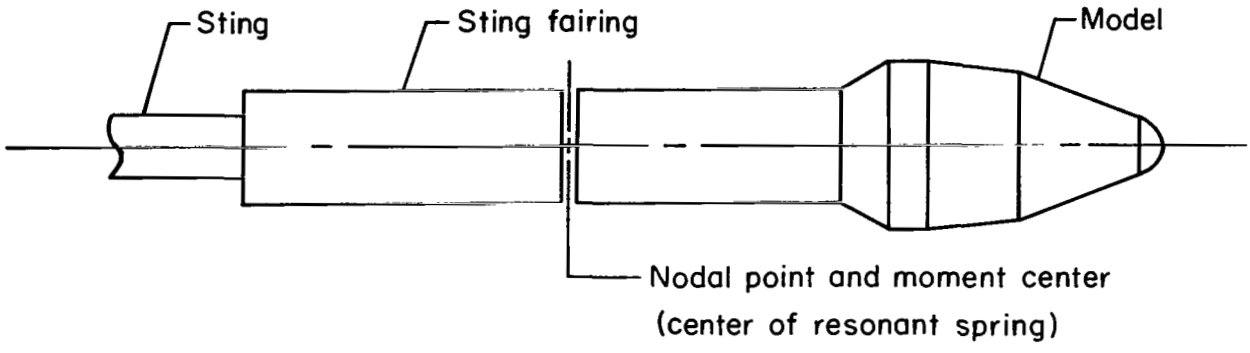

(a) Schematic drawing of the mounting system.

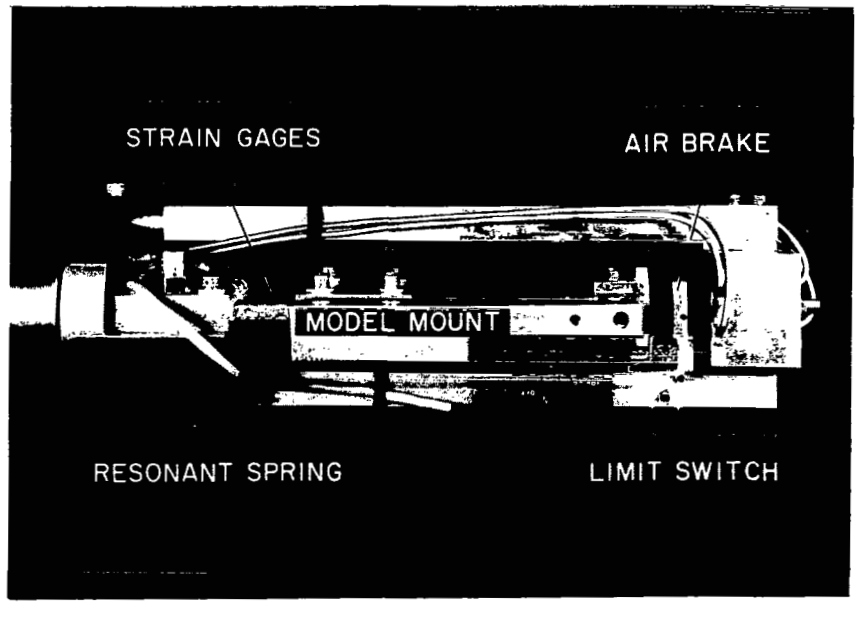

(b) Details of the free-oscillation balance.

Figure 6.- The method of mounting the models on the sting.

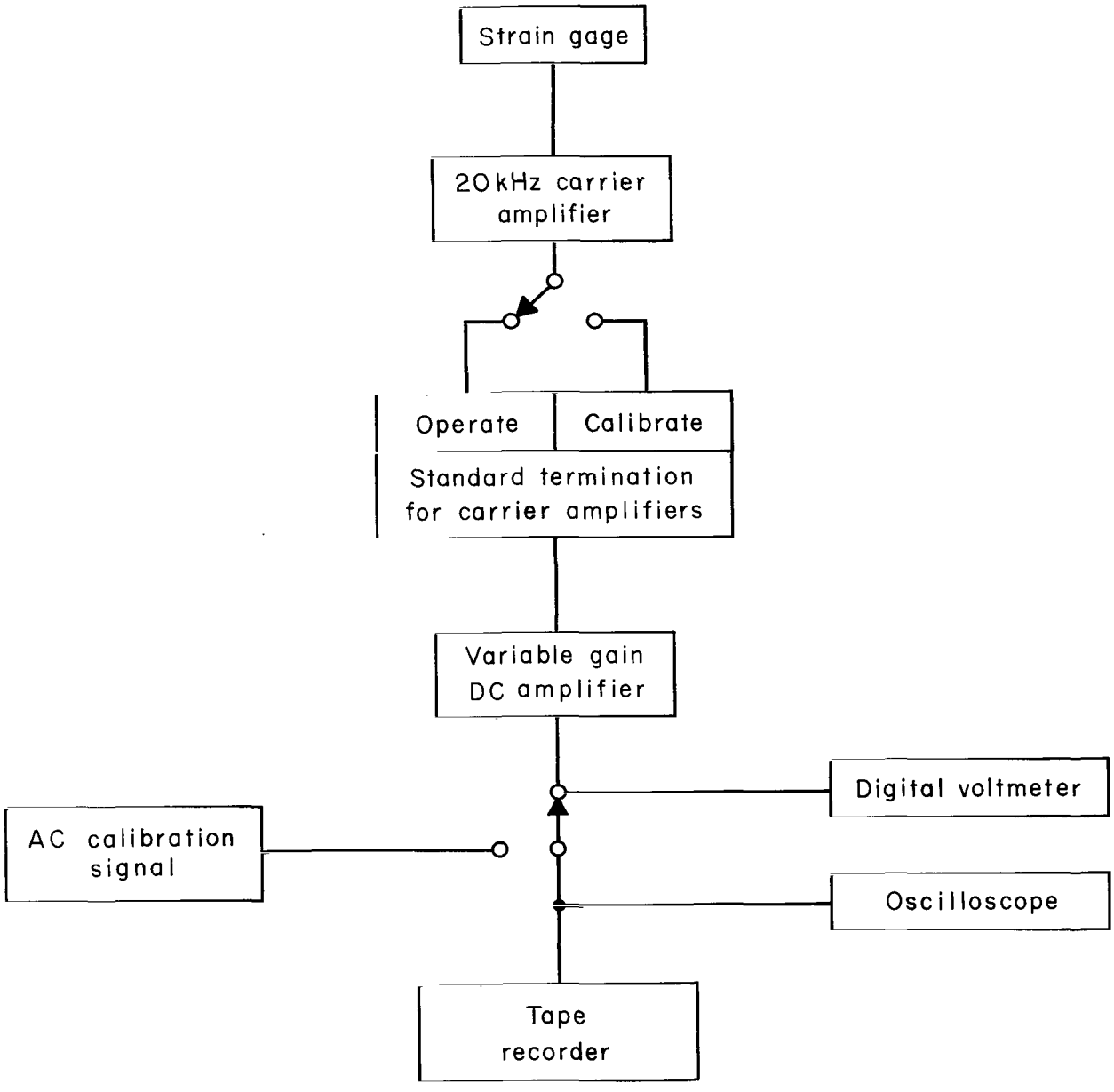

Figure 7.- Instrumentation used in recording the response of the models.

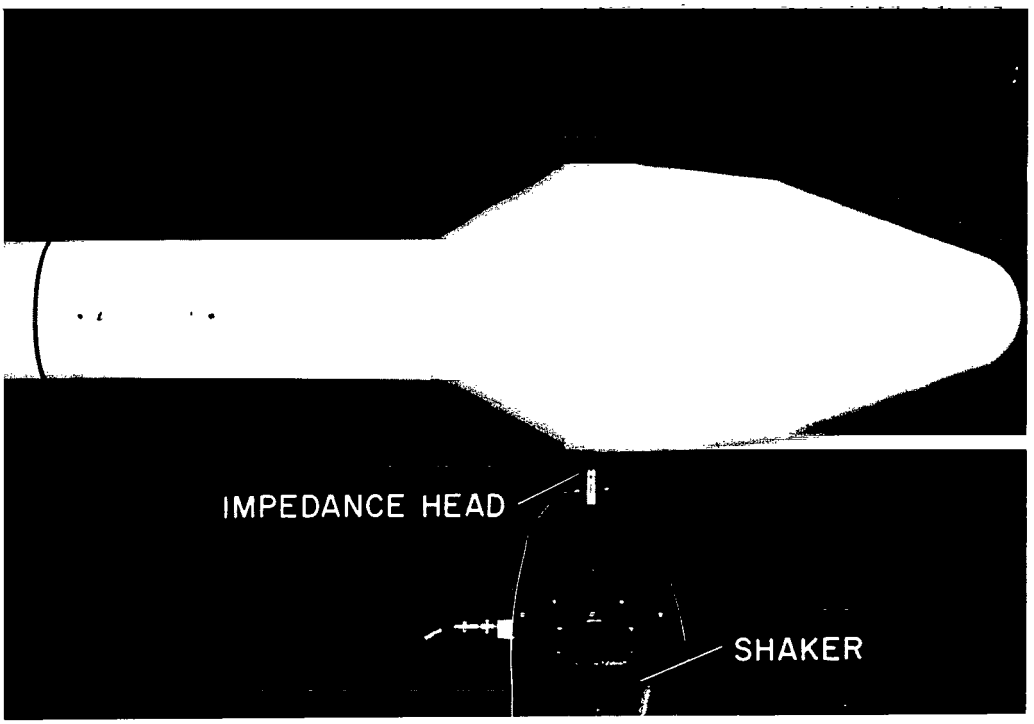

A-35375.1

Figure 8.- Shaker installation for wind-off tests.

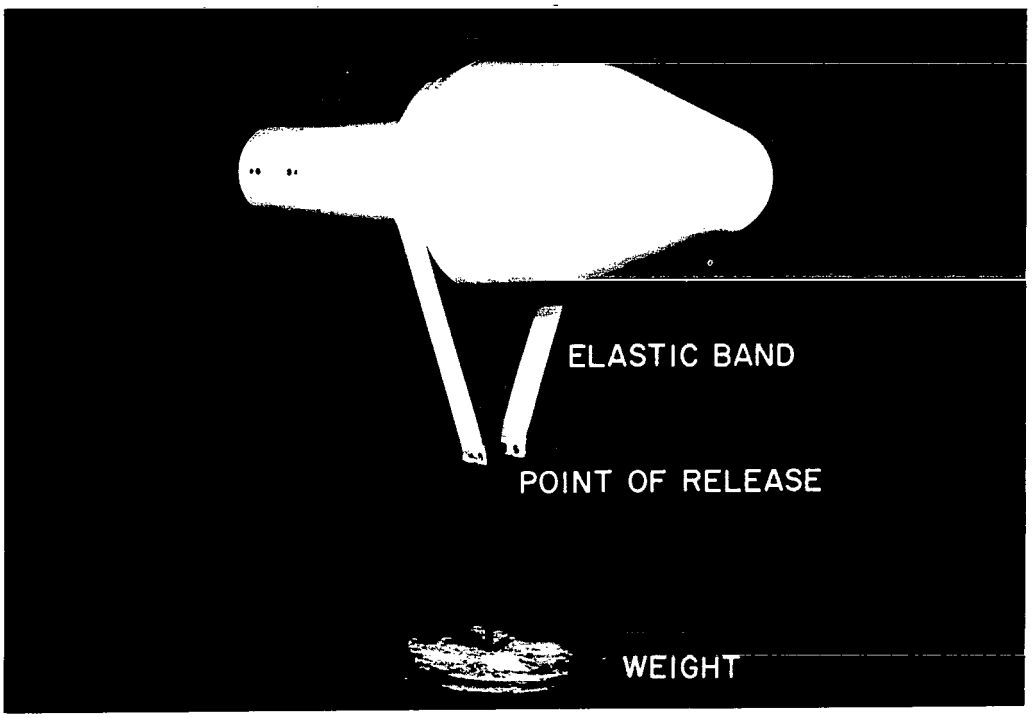

A-35595.1

Figure 9.- The technique used to produce a step input for initiating free oscillations.

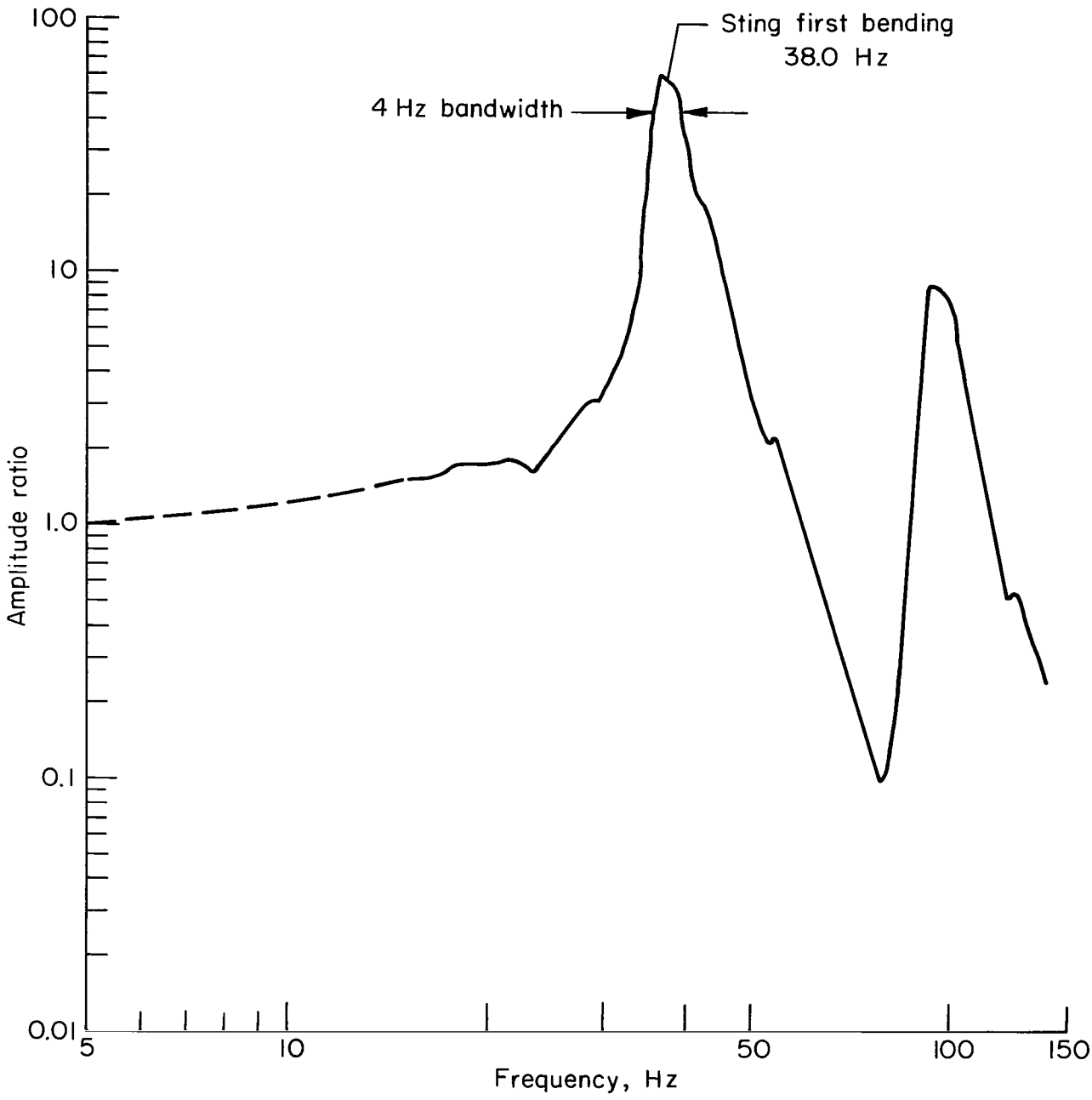

Figure 10.- The frequency response of a sting used in the 11-foot wind tunnel.

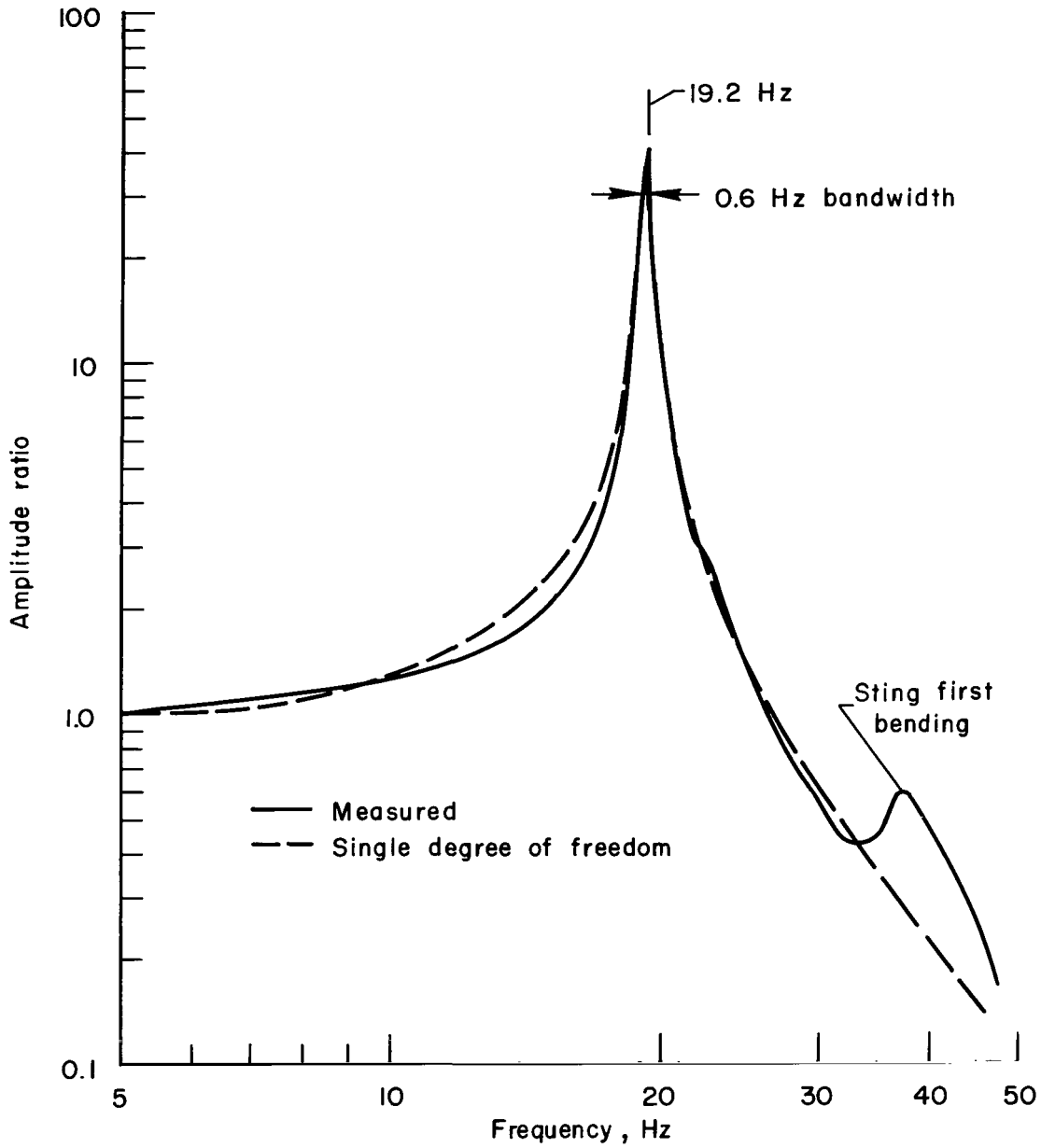

Figure 11.- The wind-off frequency response of the D/d = 2.0, $\delta = 30^{\circ}$ model mounted in the 11-foot wind tunnel.

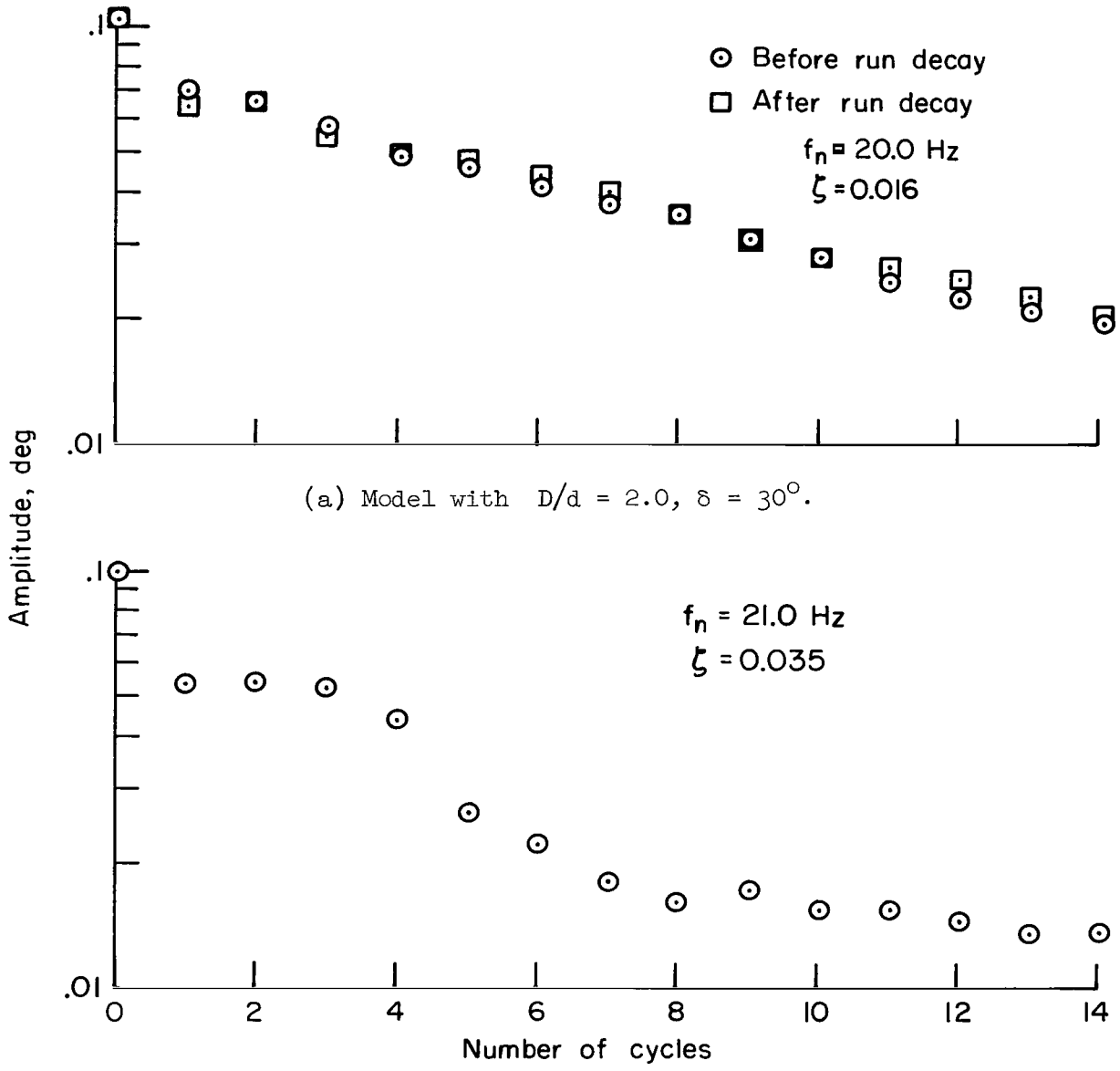

(a) Model with D/d = 2.0, δ = 30°.

(b) Model with D/d = 1.6, δ = 25°.

Figure 12.- The effect of a small change in frequency on the free-oscillation decay.

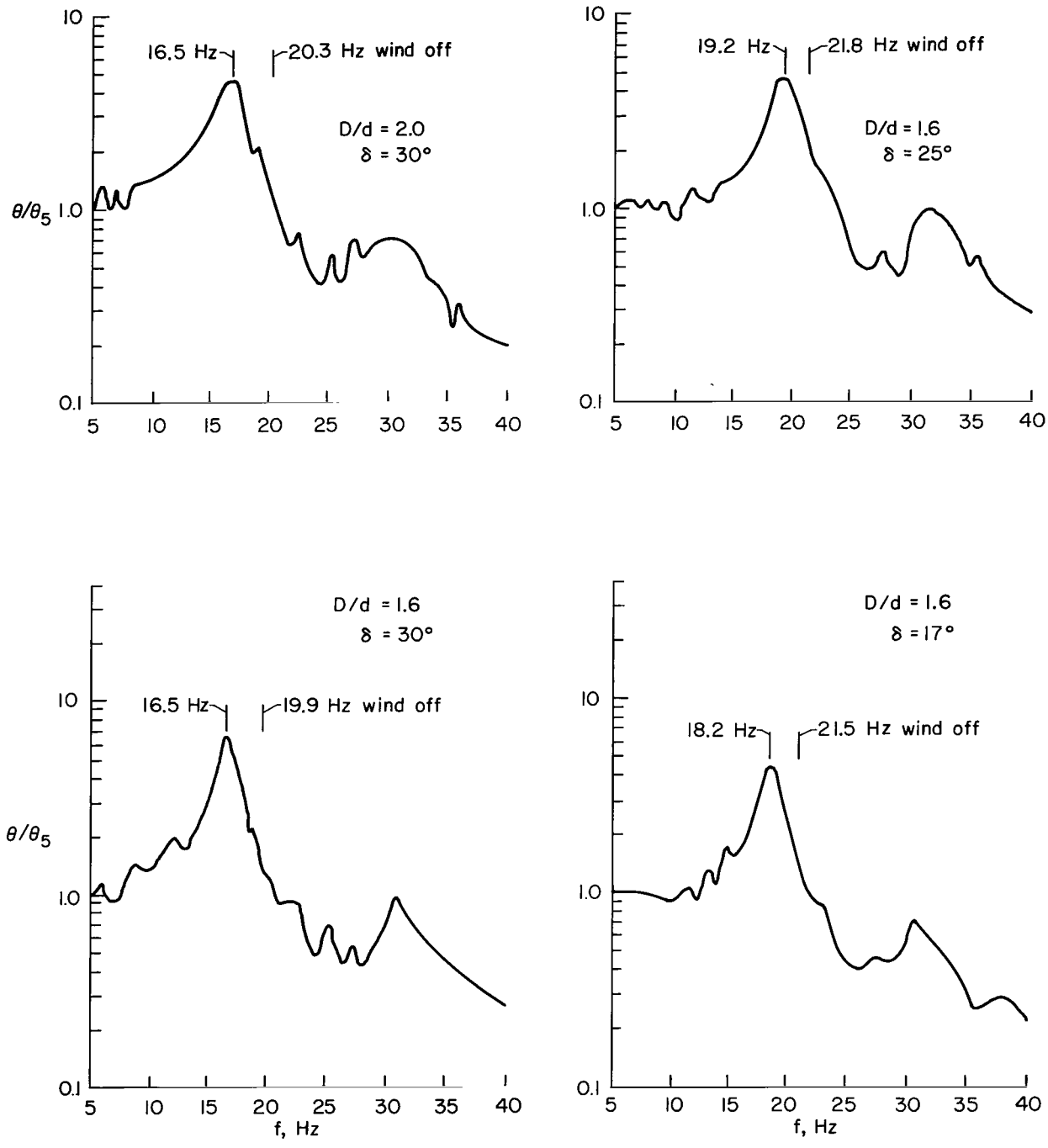

(a) M = 0.95, α = 0.

Figure 13.- Typical wind-on amplitude spectra for four models at two Mach numbers.

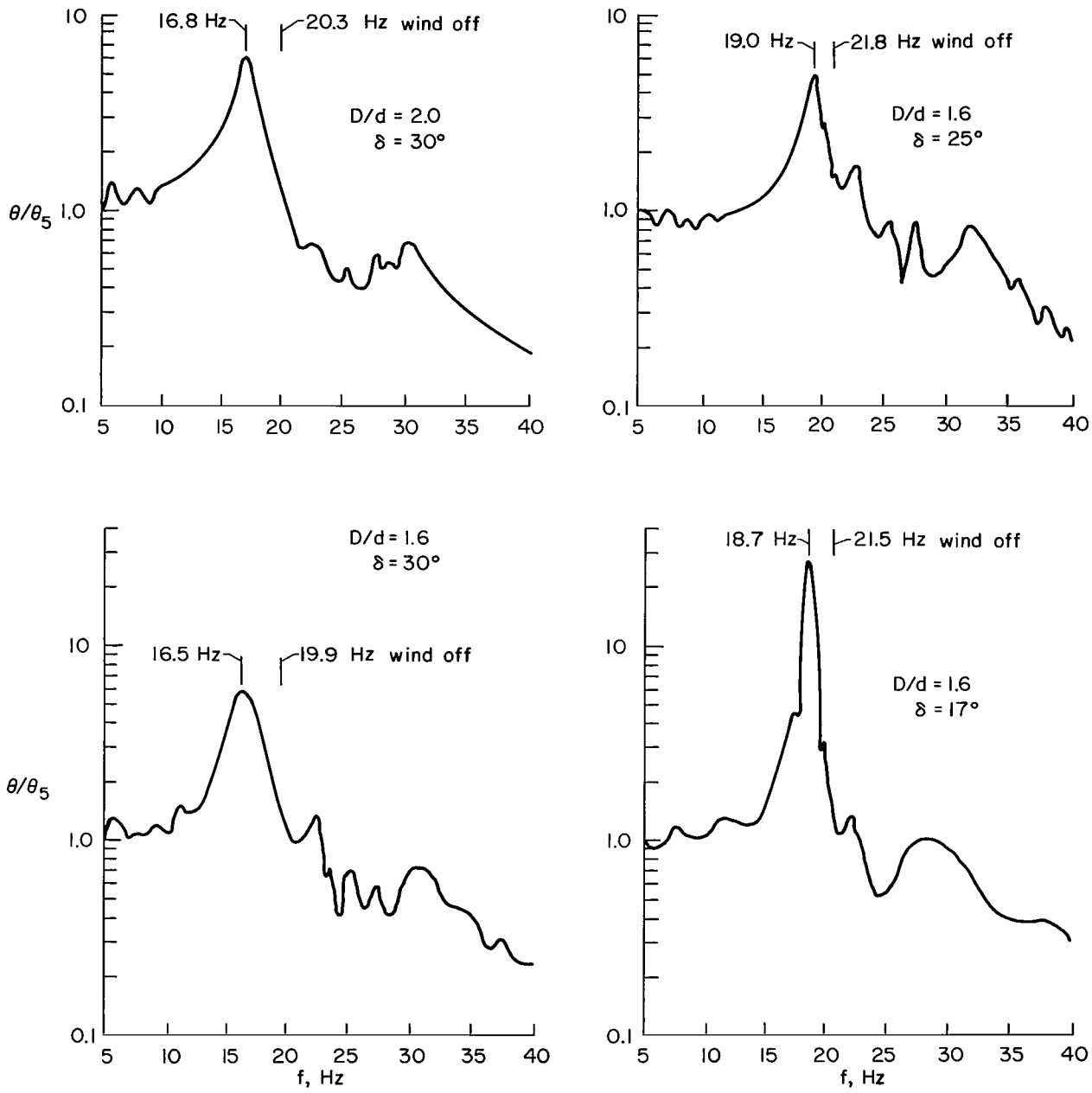

(b) M = 1.00, α = 0.

Figure 13.- Concluded.

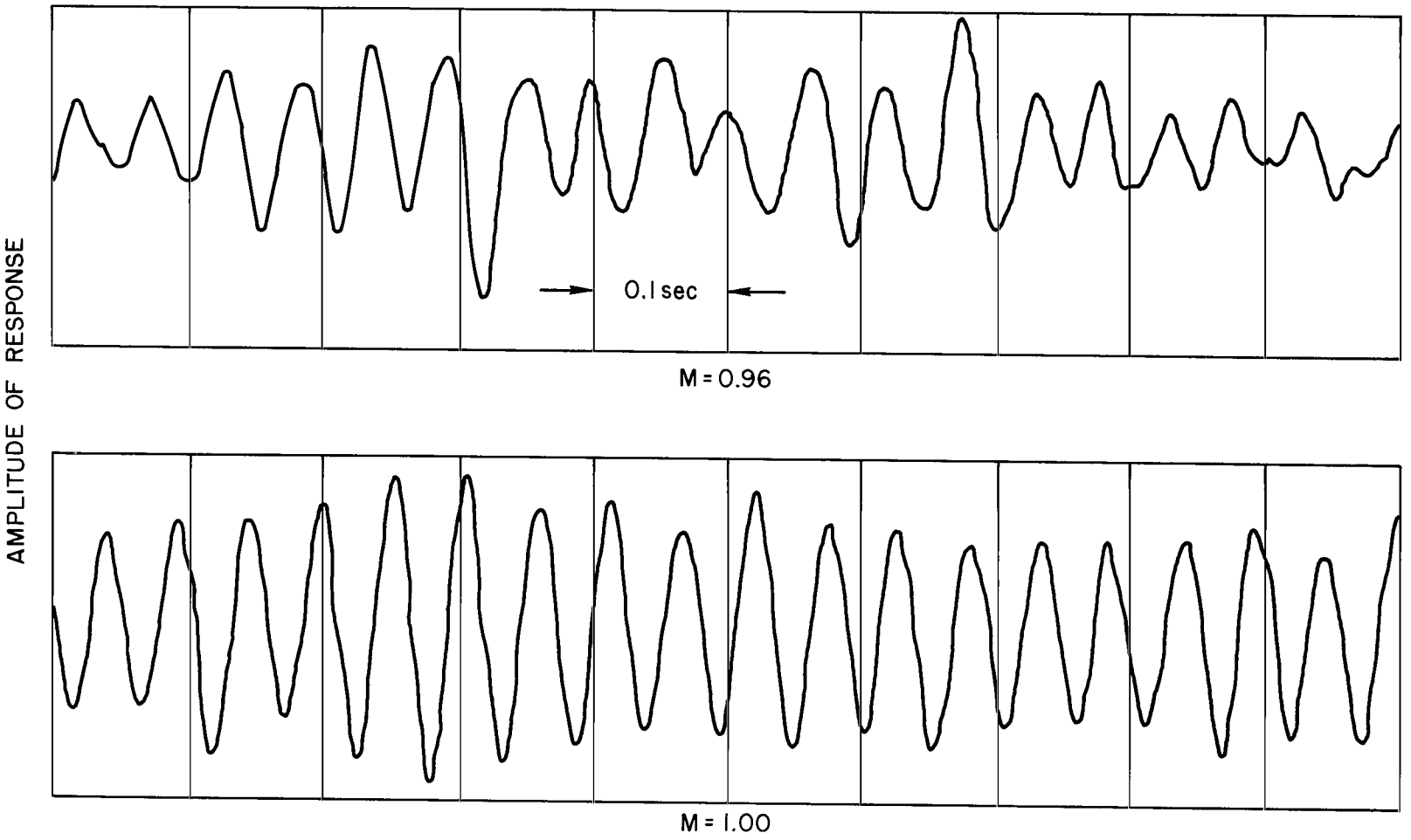

Figure 14.- Time histories of the response of the $D/d = 1.6$, $\delta = 17^{\circ}$ model at $\alpha = 0$.

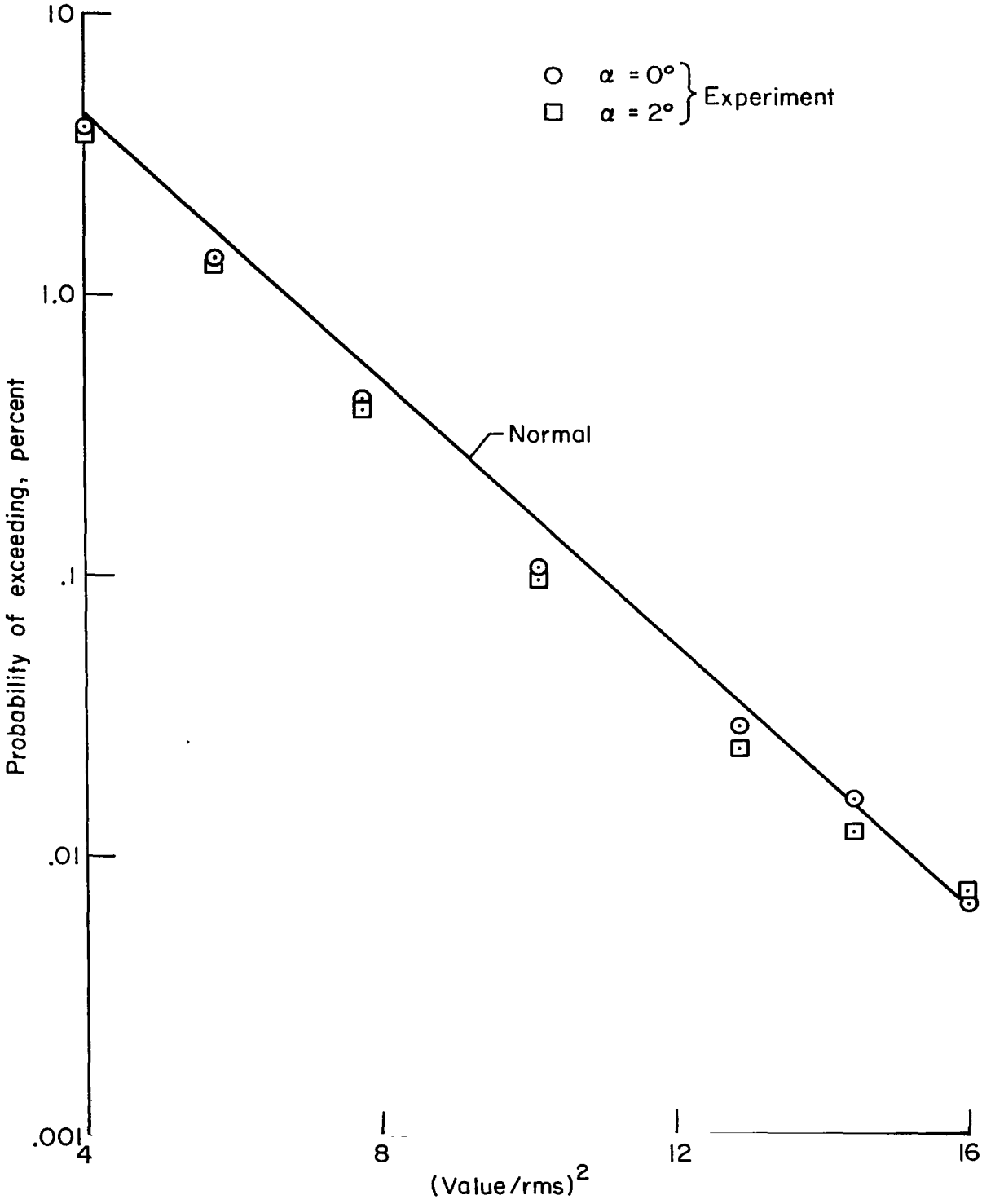

Figure 15.- Distribution of points on the time histories.

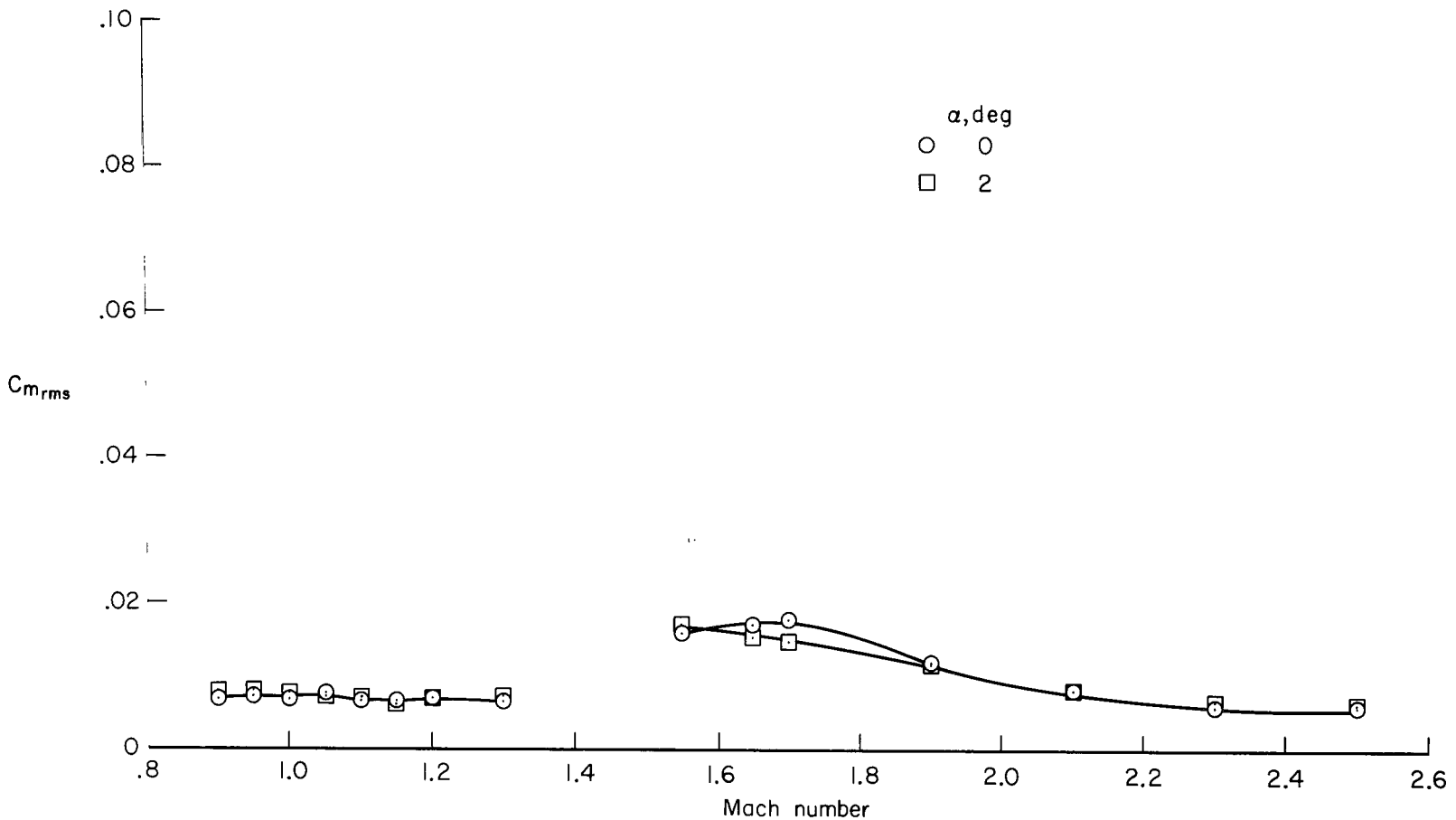

Figure 16.- Variation of the moment coefficient with Mach number for the D/d = 1.10, δ = 30° model.

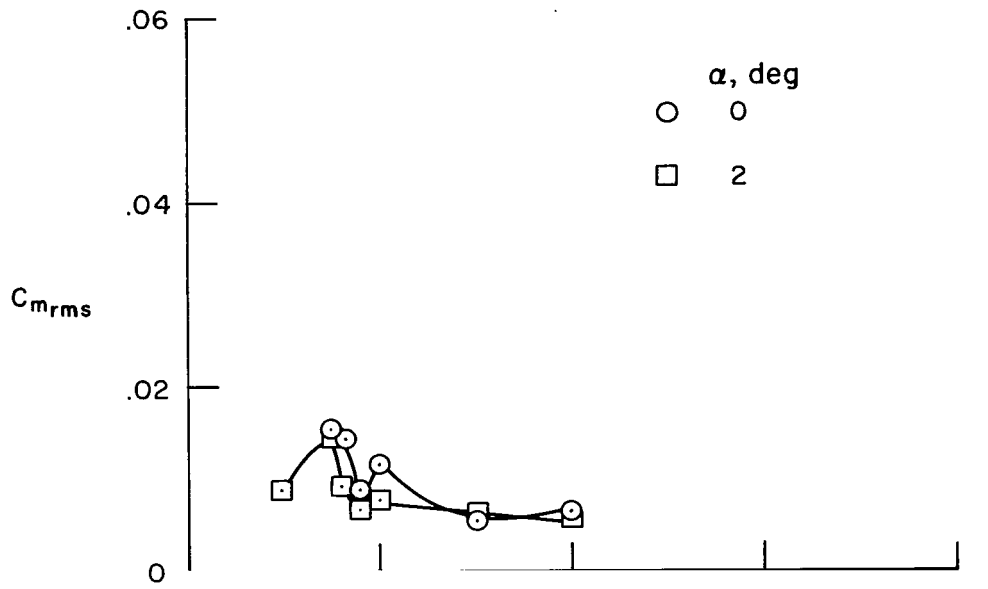

(a) $\delta = 17^{\circ}$

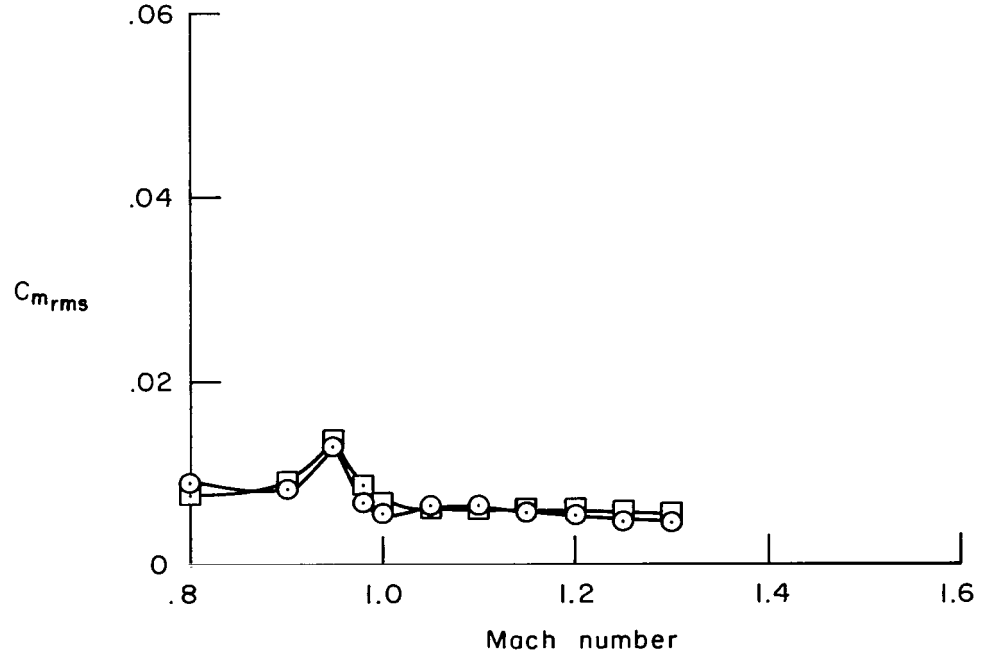

(b) $\delta = 20^{\circ}$

Figure 17.- Variation of the moment coefficient with Mach number for the models with D/d = 1.25.

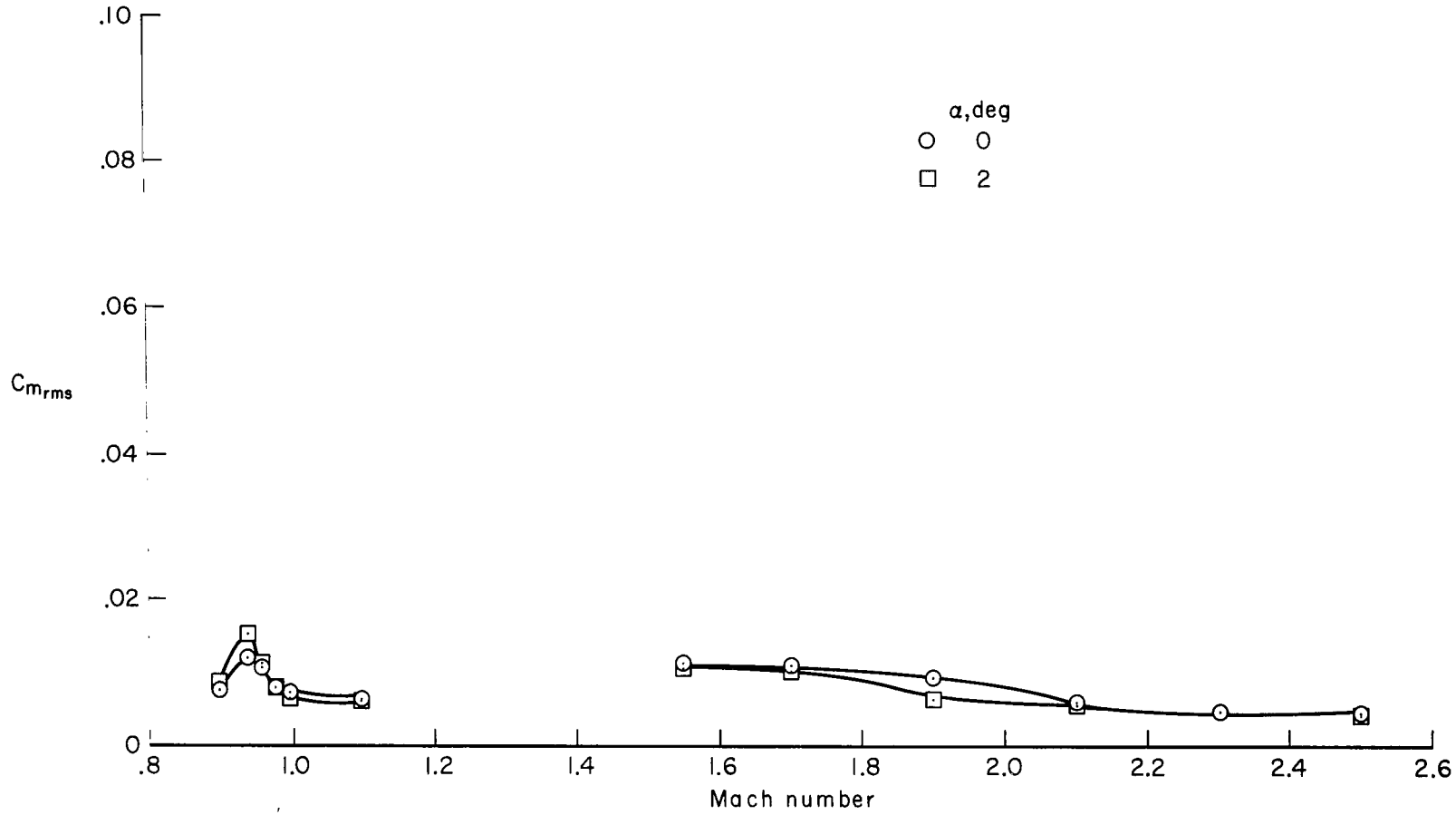

(c) $\delta = 30^{\circ}$

Figure 17.- Concluded.

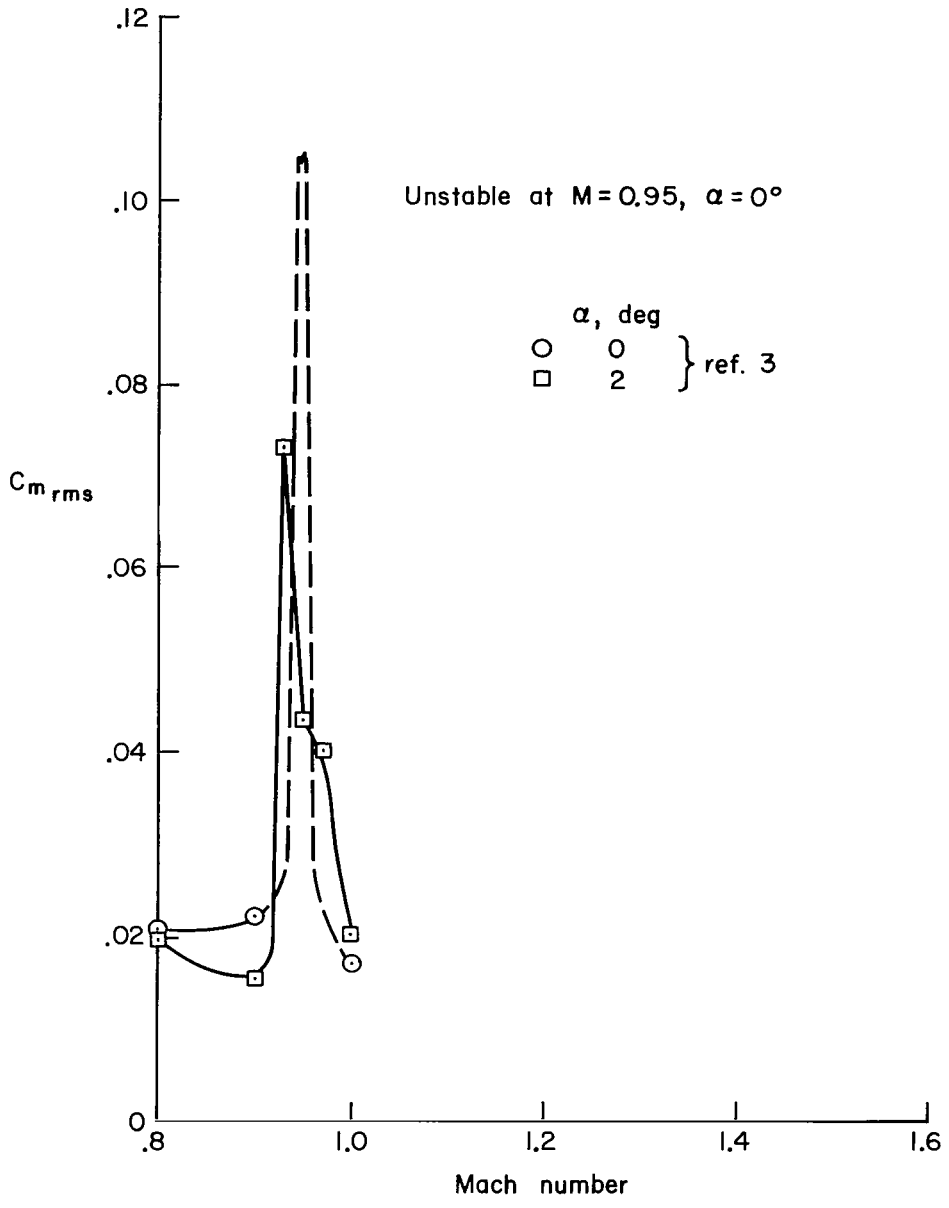

(a) $\delta = 10^{\circ}$

Figure 18.- Variation of moment coefficient with Mach number for models with D/d = 1.6.

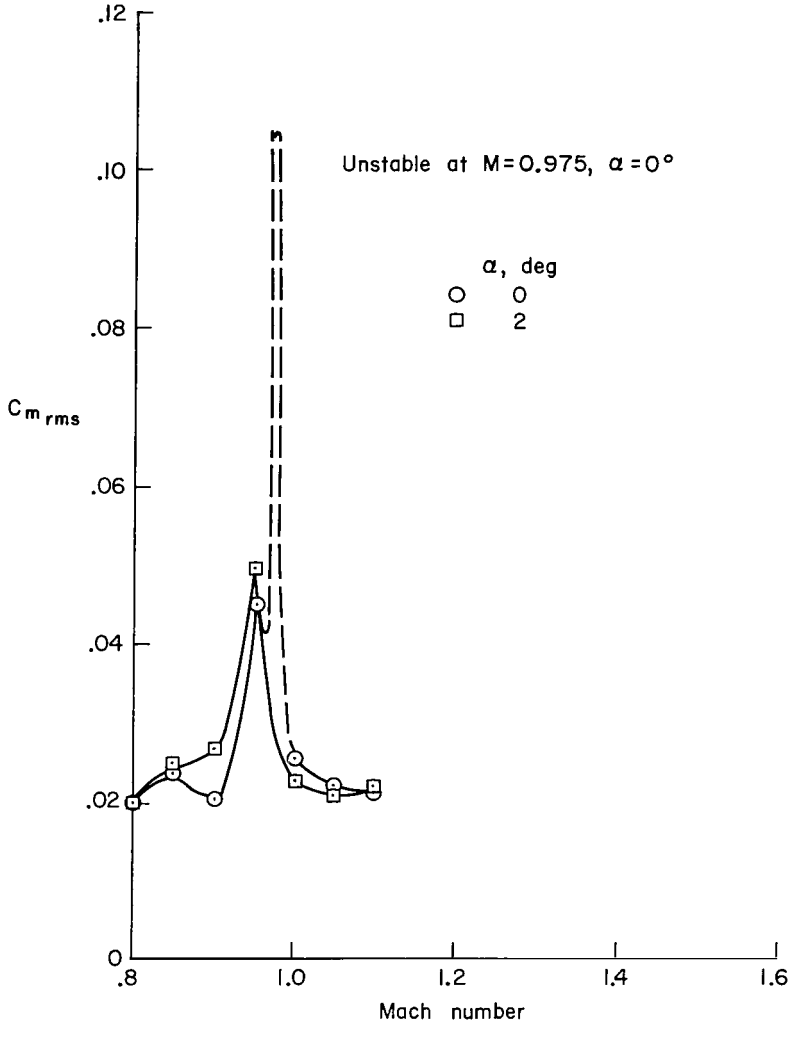

(b) $\delta = 15^{\circ}$

Figure 18.- Continued.

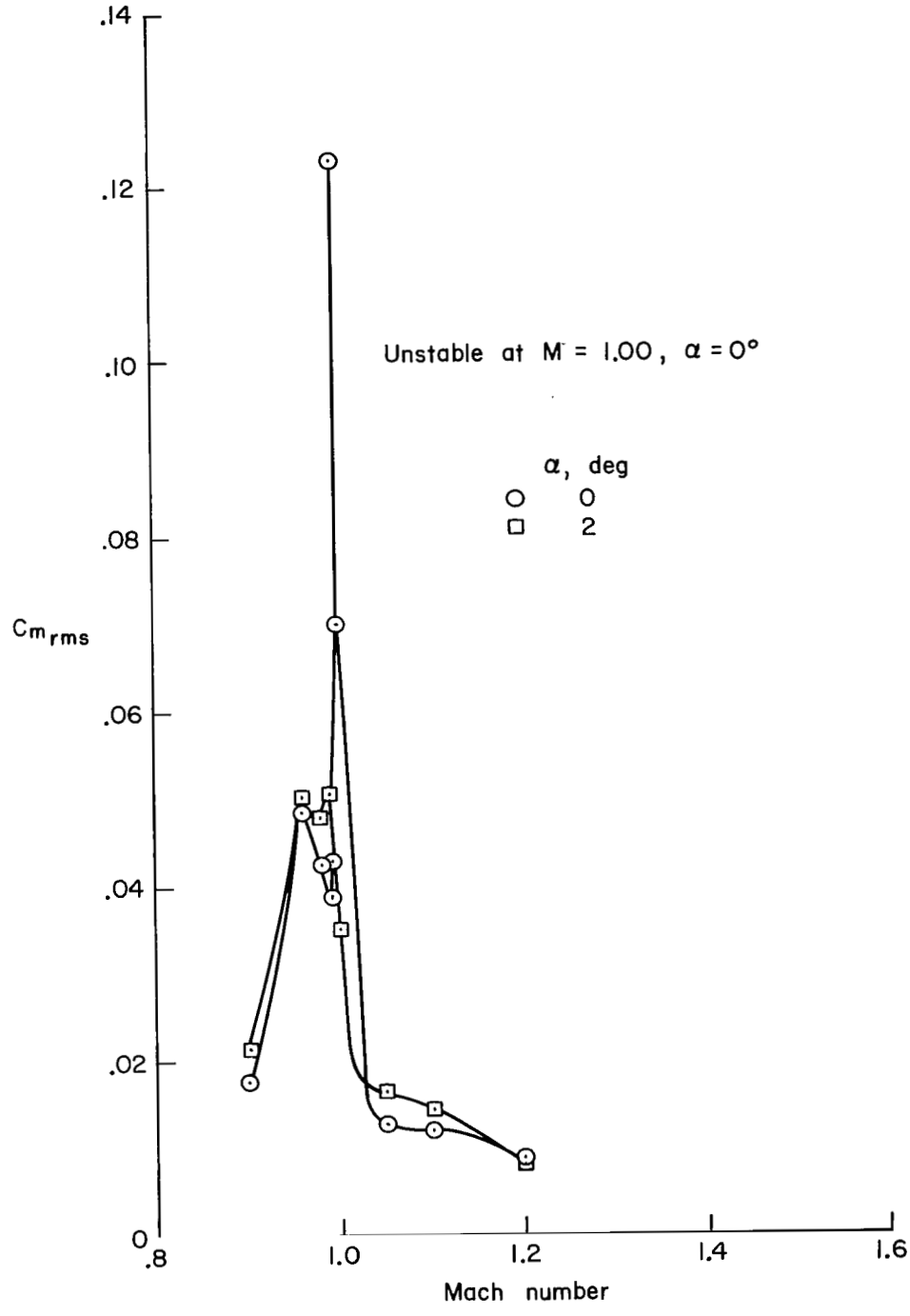

(c) $\delta = 17^{\circ}$

Figure 18.- Continued.

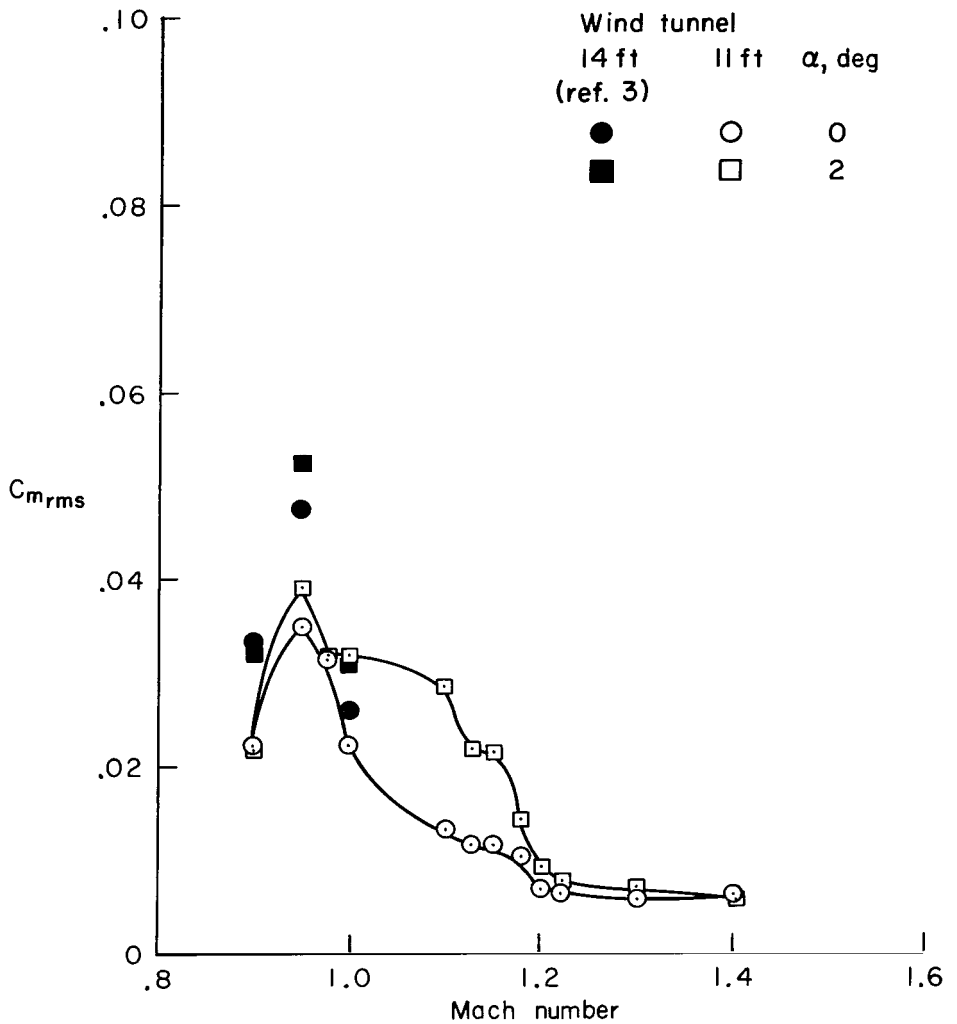

(d) $\delta = 20^{\circ}$

Figure 18.- Continued.

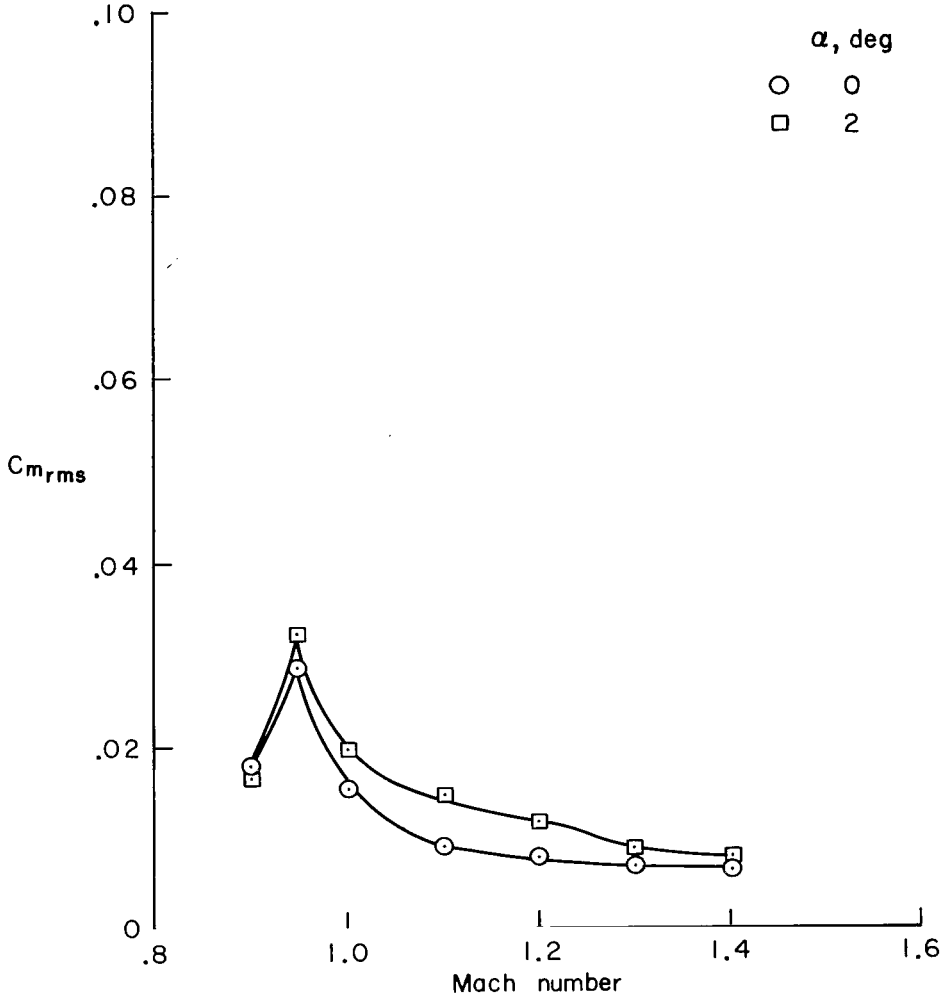

(e) $\delta = 25^{\circ}$

Figure 18.- Continued.

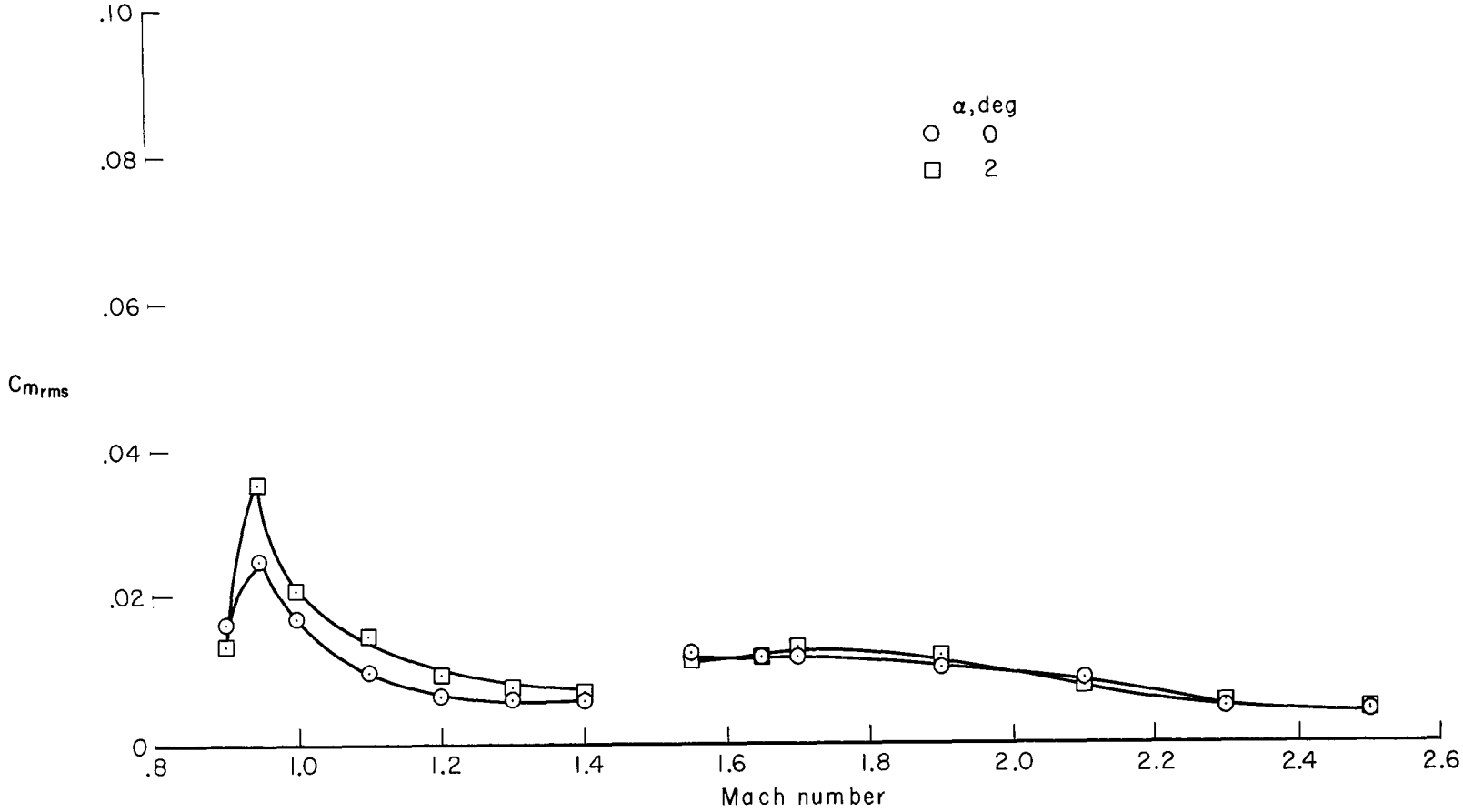

(f) $\delta = 30^{\circ}$

Figure 18.- Concluded.

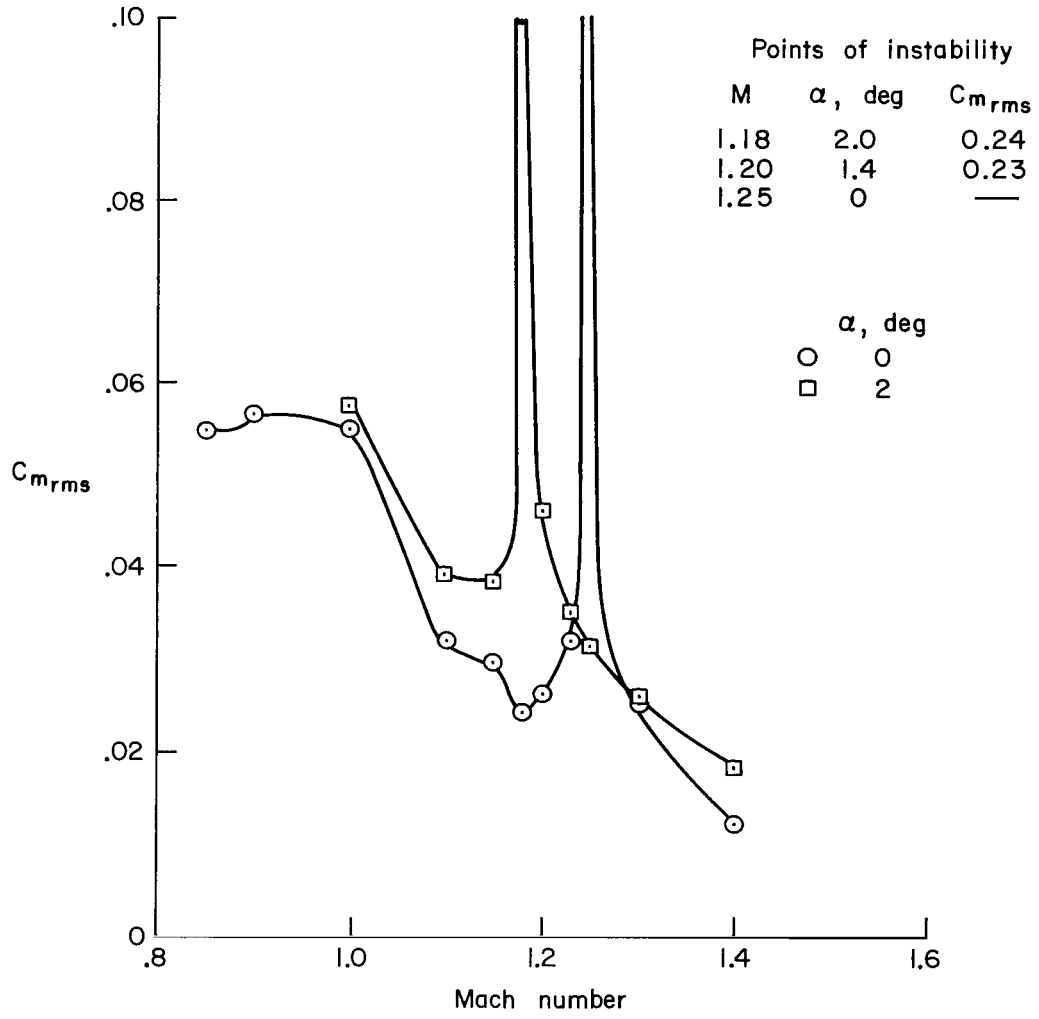

(a) $\delta = 20^{\circ}$

Figure 19.- Variation of moment coefficient with Mach number for the models with D/d = 2.0.

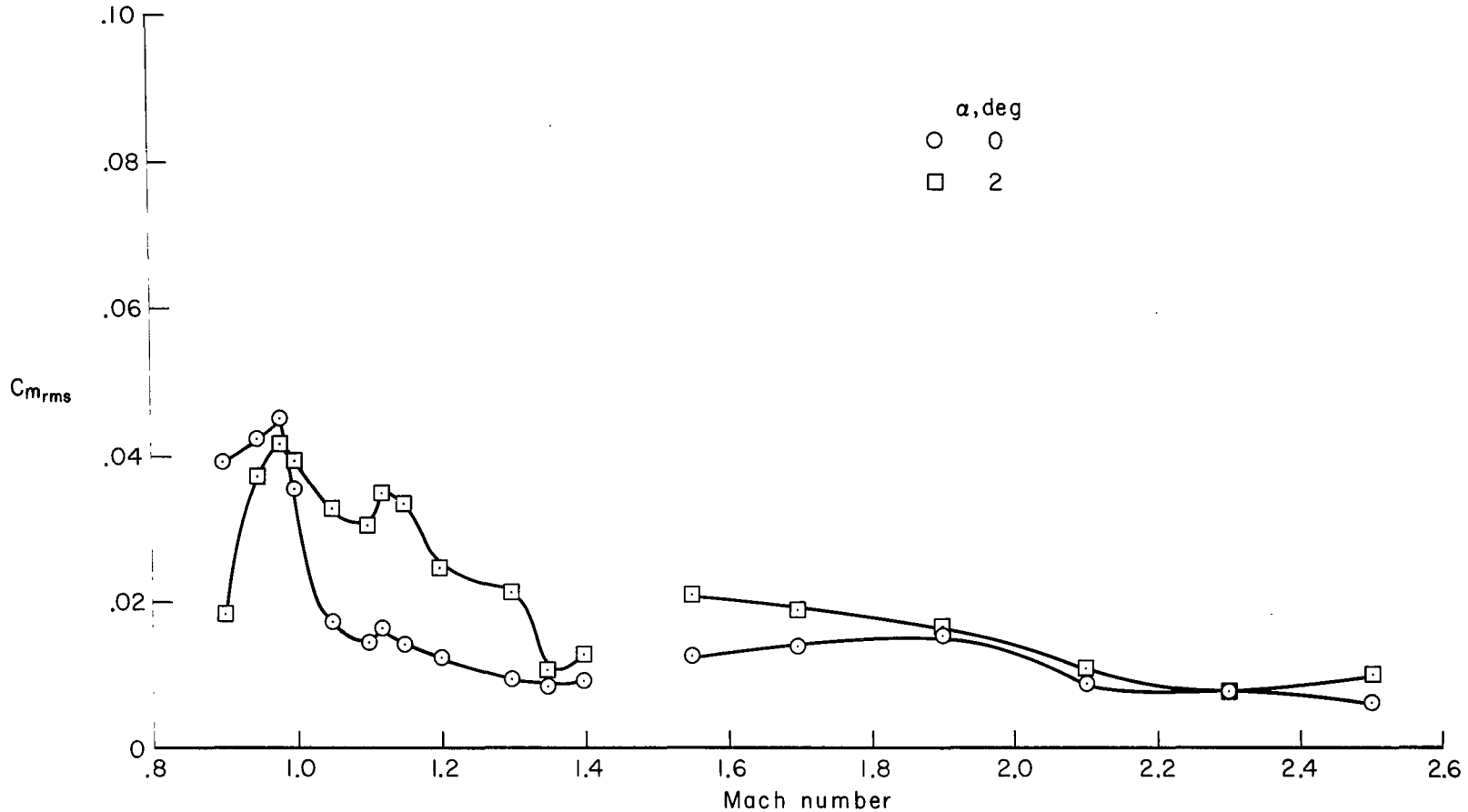

(b) $\delta = 25^{\circ}$

Figure 19.- Continued.

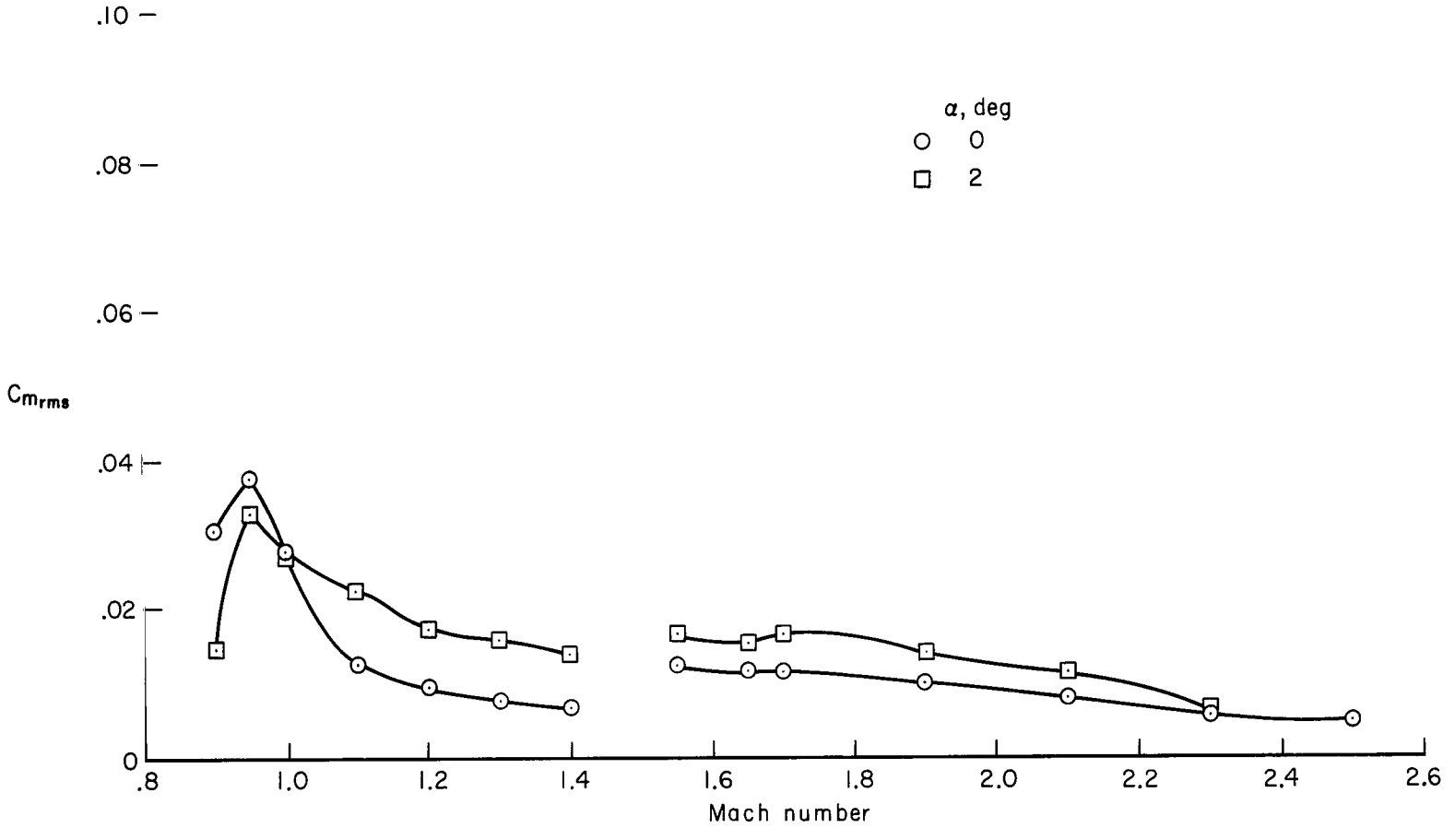

(c) $\delta = 30^{\circ}$

Figure 19.- Concluded.

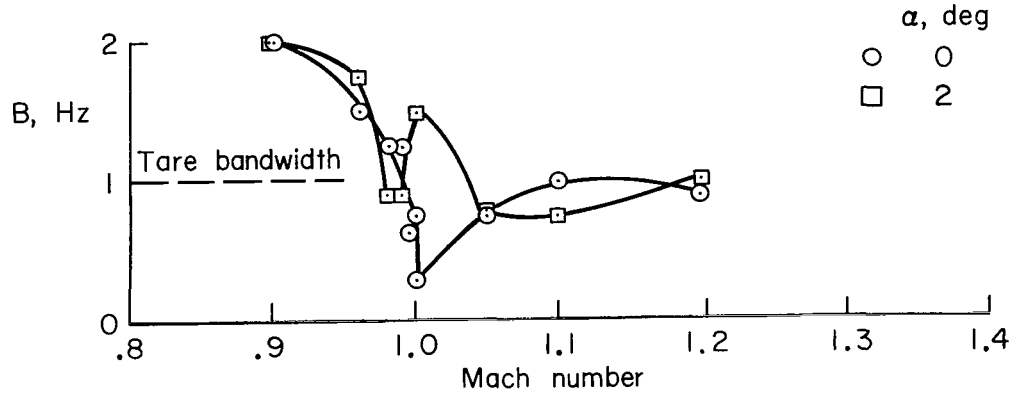

Figure 20.- The variation of bandwidth with Mach number for the D/d = 1.6, $\delta = 17^{\circ}$ model.

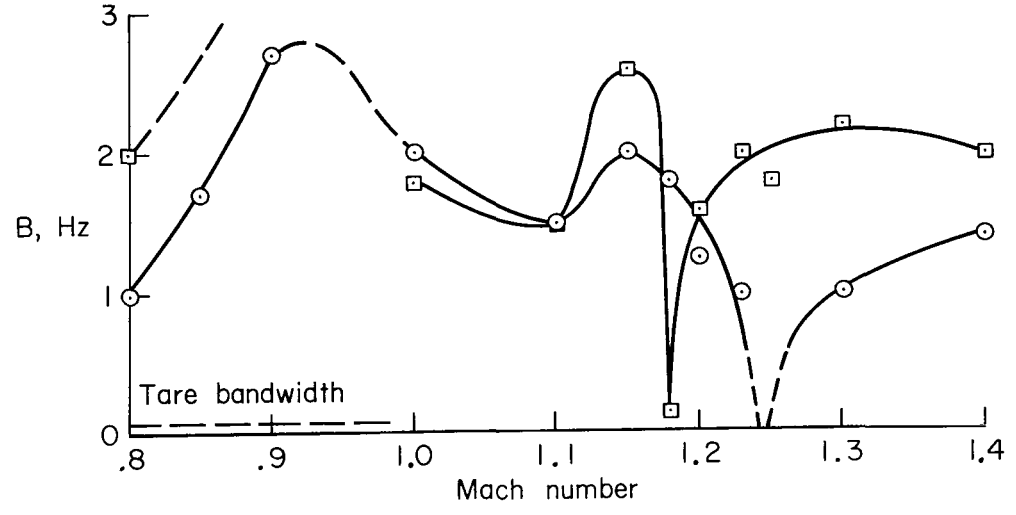

Figure 21.- The variation of bandwidth with Mach number for the D/d = 2.0, $\delta = 20^{\circ}$ model.

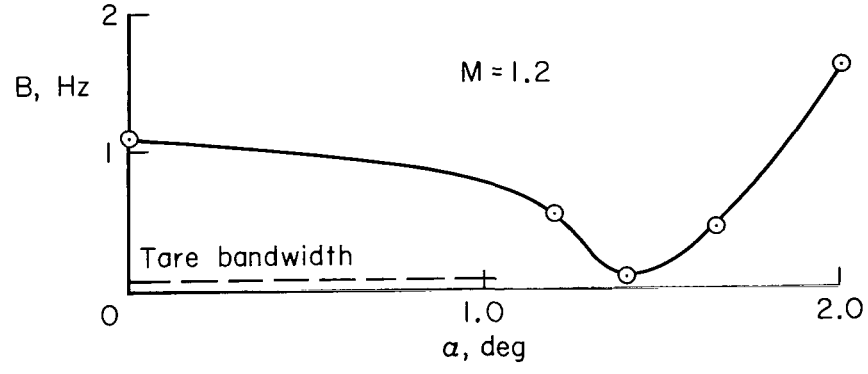

Figure 22.- The variation of bandwidth with angle of attack at M = 1.20 for the D/d = 2.0, $\delta = 20^{\circ}$ model.

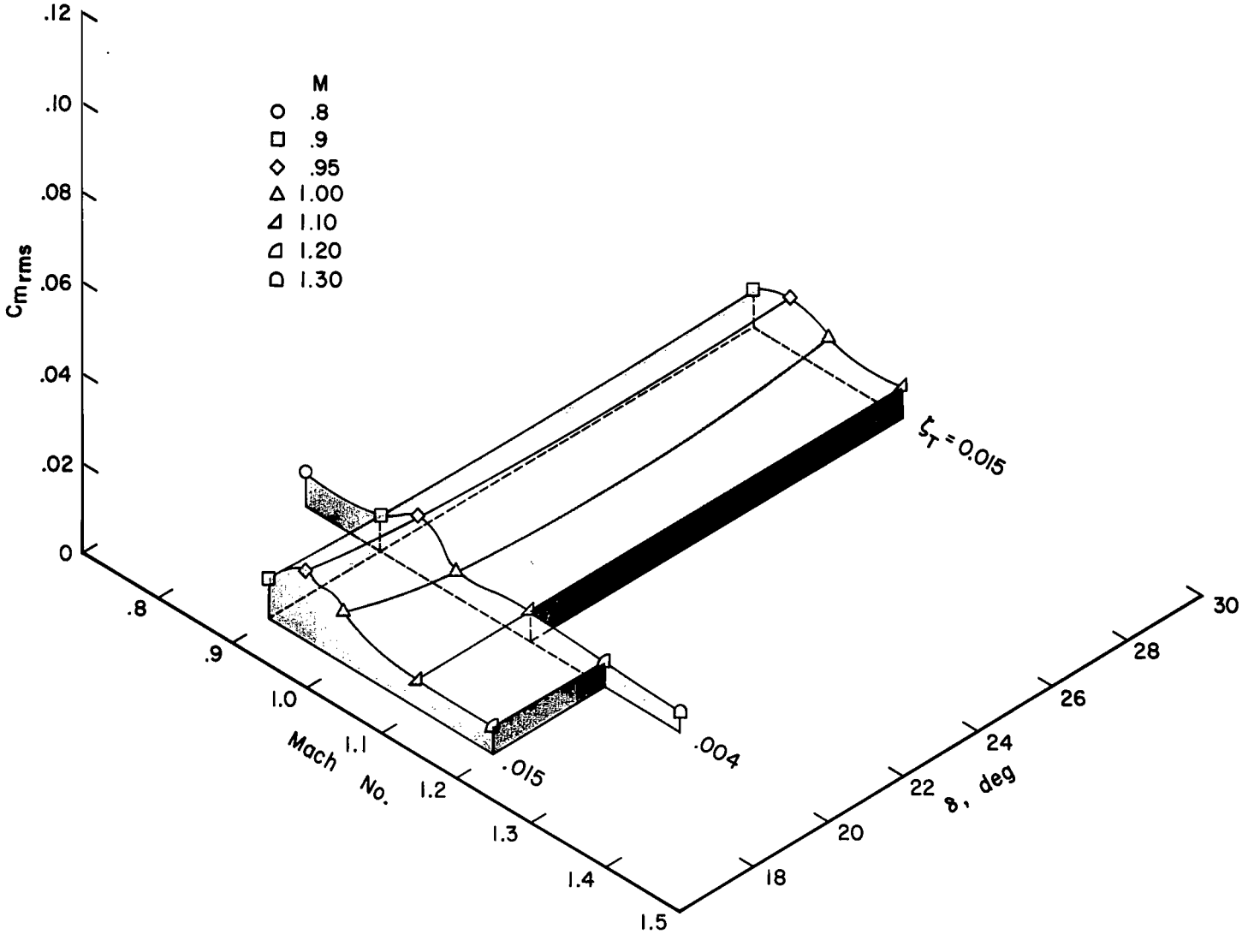

(a) D/d = 1.25

Figure 23.- Model response as a function of Mach number and boattail angle with diameter ratio constant, α = 0.

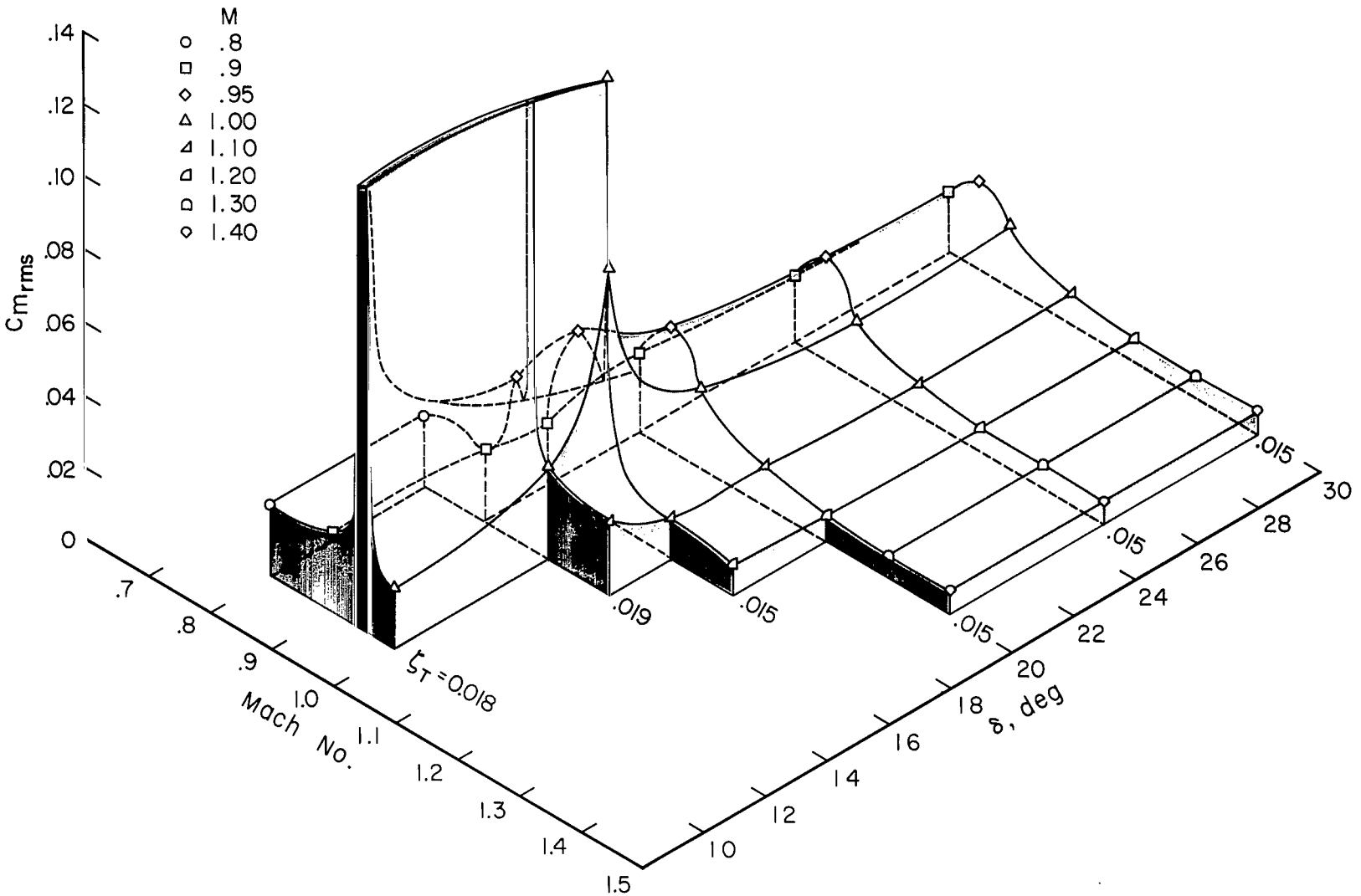

(b) D/d = 1.6

Figure 23.- Continued.

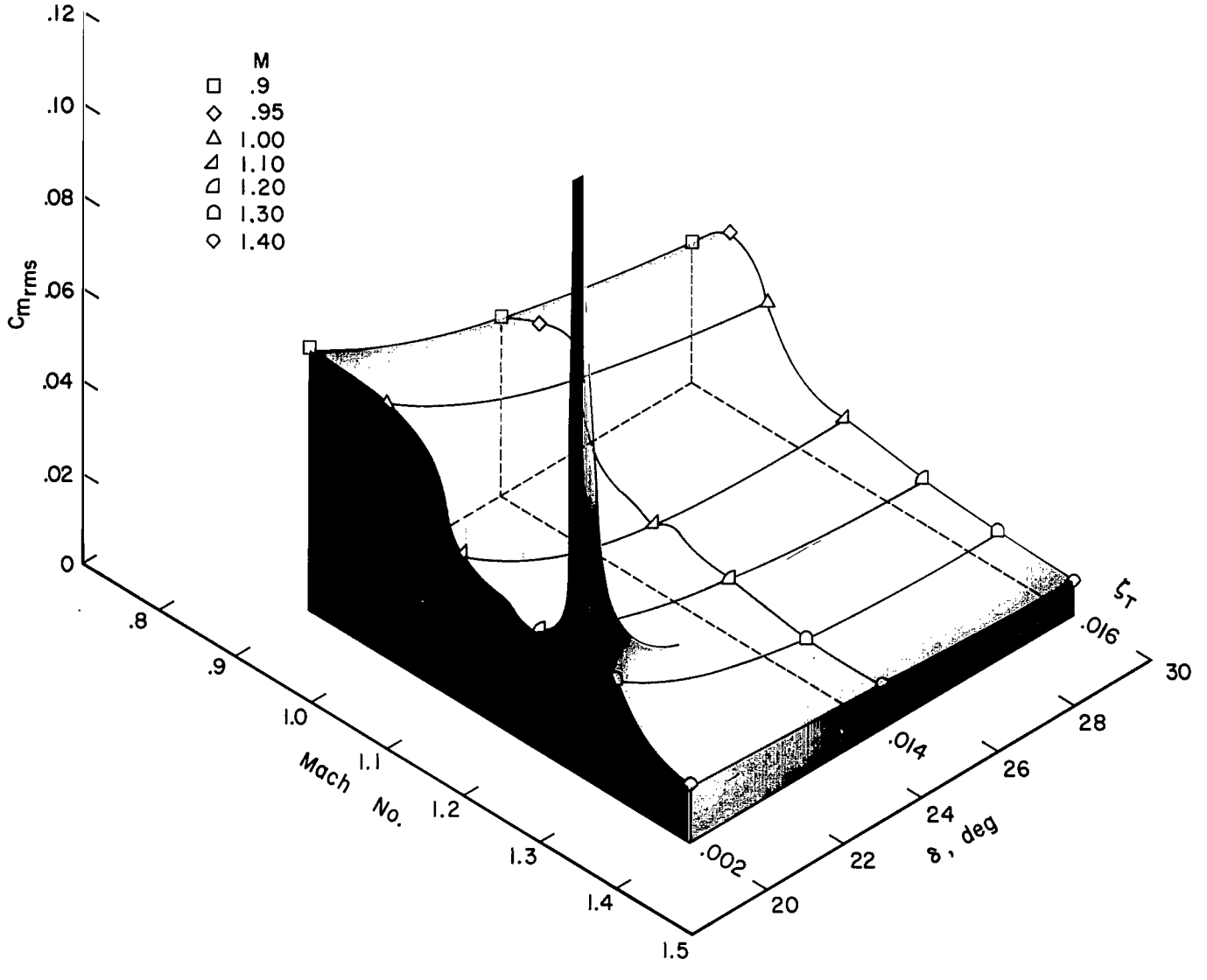

(c) D/d = 2.00

Figure 23.- Concluded.

"The aeronautical and space activities of the United States shall be conducted so as to contribute . . . to the expansion of human knowledge of phenomena in the atmosphere and space. The Administration shall provide for the widest practicable and appropriate dissemination of information concerning its activities and the results thereof."

—NATIONAL AERONAUTICS AND SPACE ACT OF 1958

NASA SCIENTIFIC AND TECHNICAL PUBLICATIONS

TECHNICAL REPORTS: Scientific and technical information considered important, complete, and a lasting contribution to existing knowledge.

TECHNICAL NOTES: Information less broad in scope but nevertheless of importance as a contribution to existing knowledge.

TECHNICAL MEMORANDUMS: Information receiving limited distribution because of preliminary data, security classification, or other reasons.

CONTRACTOR REPORTS: Scientific and technical information generated under a NASA contract or grant and considered an important contribution to existing knowledge.

TECHNICAL TRANSLATIONS: Information published in a foreign language considered to merit NASA distribution in English.

SPECIAL PUBLICATIONS: Information derived from or of value to NASA activities. Publications include conference proceedings, monographs, data compilations, handbooks, sourcebooks, and special bibliographies.

TECHNOLOGY UTILIZATION PUBLICATIONS: Information on technology used by NASA that may be of particular interest in commercial and other non-aerospace applications. Publications include Tech Briefs, Technology Utilization Reports and Notes, and Technology Surveys.

Details on the availability of these publications may be obtained from:

SCIENTIFIC AND TECHNICAL INFORMATION DIVISION

NATIONAL AERONAUTICS AND SPACE ADMINISTRATION

Washington, D.C. 20546